How Do Environmental Conditions Influence Vertical Buoyancy Structure and Shallow-to-Deep Convection Transition across Different Climate Regimes?

YIZHOU ZHUANG

Department of Atmospheric and Oceanic Sciences, School of Physics, Peking University, Beijing, China, and Department of Atmospheric and Oceanic Sciences, University of California, Los Angeles, Los Angeles, California

RONG FU

Department of Atmospheric and Oceanic Sciences, University of California, Los Angeles, Los Angeles, California

HONGQING WANG

Department of Atmospheric and Oceanic Sciences, School of Physics, Peking University, Beijing, China

(Manuscript received 22 September 2017, in final form 27 February 2018)

ABSTRACT

We developed an entraining parcel approach that partitions parcel buoyancy into contributions from different processes (e.g., adiabatic cooling, condensation, freezing, and entrainment). Applying this method to research-quality radiosonde profiles provided by the Atmospheric Radiation Measurement (ARM) program at six sites, we evaluated how atmospheric thermodynamic conditions and entrainment influence various physical processes that determine the vertical buoyancy structure across different climate regimes as represented by these sites. The differences of morning buoyancy profiles between the deep convection (DC)/transition cases and shallow convection (SC)/nontransition cases were used to assess preconditions important for shallow-to-deep convection transition. Our results show that for continental sites such as the U.S. Southern Great Plains (SGP) and west-central Africa, surface conditions alone are enough to account for the buoyancy difference between DC and SC cases, although entrainment further enhances the buoyancy difference at SGP. For oceanic sites in the tropical west Pacific, humidity dilution in the lower to middle free troposphere (~1–6 km) and temperature mixing in the middle to upper troposphere (>4 km) have the most important influences on the buoyancy difference between DC and SC cases. For the humid central Amazon region, entrainment in both the boundary layer and the lower free troposphere (~0–4 km) have significant contributions to the buoyancy difference; the upper-tropospheric influence seems unimportant. In addition, the integral of the condensation term, which represents the parcel's ability to transform available water vapor into heat through condensation, provides a better discrimination between DC and SC cases than the integral of buoyancy or the convective available potential energy (CAPE).

1. Introduction

Convection and its associated precipitation systems play a central role in regulating the local and global atmospheric circulation and the water–energy balance. Representation of convection in global climate models (GCMs) remains a challenging problem, especially in the tropics (Anber et al. 2015). A common deficiency of many GCMs involves the incorrect diurnal cycle of cloud and precipitation, which is often linked to the models' inability to simulate a smooth shallow-to-deep convection transition (e.g., Rieck et al. 2014; Stratton and Stirling 2012; Yang and Smith 2006). Efforts have been devoted to investigating this transition process from the viewpoint of the diurnal cycle using model simulations (Grabowski et al. 2006; Guichard et al. 2004; Wu et al. 2009). In addition, studies of the preconditions for both shallow and deep convection using observational data can also help us understand the environmental conditions central to triggering the shallow-to-deep convection transition (Zhang and Klein 2010; Zhuang et al. 2017). Many previous studies have related the shallow-to-deep convection transition to a more humid lower troposphere in both continental and oceanic regions

Corresponding author: Yizhou Zhuang, zyz90@pku.edu.cn

DOI: 10.1175/JAS-D-17-0284.1

(e.g., Bretherton et al. 2004; Holloway and Neelin 2009; Nuijens et al. 2009; Powell and Houze 2015; Ruppert and Johnson 2015; Schiro et al. 2016; Zhang and Klein 2010; Zhuang et al. 2017). However, what the relative influence of the atmospheric boundary layer (ABL) is versus that of the free troposphere in different climate regimes has remained unclear. In addition, the influence of surface conditions versus lateral entrainment in/above the ABL on temperature mixing, humidity dilution, and ice formation of a convective parcel in different oceanic and continental climate regimes have not yet been investigated systematically. For convective instability, parcel theory is commonly used to calculate parcel buoyancy and some derived indices, such as convective available potential energy (CAPE), convective inhibition (CIN), and lifting condensation level (LCL). Some studies have related deep convective events to a larger CAPE and smaller CIN before the transition from shallow to deep convection (e.g., Zhang and Klein 2010; Zhuang et al. 2017). However, parcel theory is a highly idealized single-column model with many assumptions. Thus, it may not adequately represent the environmental impacts on convection in all cases. One of the most important assumptions in the traditional CAPE and CIN calculations is that the parcel remains isolated from the environment; that is, the parcel has no entrainment or detrainment during its ascent. As a result, buoyancy and the related indices like CAPE can highly depend on the choice of initial parcel. For example, it was shown that in the central Amazon, there is no significant difference in surface-based CAPE (SBCAPE) between shallow and deep convection cases, but the difference becomes significant for mixed-layer CAPE (MLCAPE), which uses average temperature and humidity in the mixed layer as source parcel properties (Zhuang et al. 2017).

To address this issue, some studies have incorporated entrainment into the calculation of buoyancy and shown that the entrainment in the troposphere is important in representing the vertical buoyancy profile needed for the development of deep convection (e.g., Holloway and Neelin 2009; Schiro et al. 2016). However, these studies have focused on tropical oceanic and humid continental climate regimes without explicitly partitioning the influences of lateral entrainment on various physical processes and their contributions to the total buoyancy.

This work, inspired by the abovementioned studies, aims to clarify the thermodynamic preconditions for the shallow-to-deep convection transition and how they vary in different climate regimes, that is, interior subtropical continent, monsoonal tropical continent, humid tropical continent, and humid tropical ocean. Our approach is as follows:

1) Develop a convective parcel model that decomposes buoyancy changes into contributions from various physical processes such as dry adiabatic cooling, condensation, freezing, and entrainment at different levels. In doing so, we can link variations of the environmental conditions to processes that determine the parcel buoyancy.
2) Use the buoyancy difference derived from morning soundings between the days when shallow convection grew into deep convection in the afternoon (DC cases), and the days when the shallow convection stayed shallow (SC cases) to assess the thermodynamic preconditions favorable for a shallow-to-deep convection transition.
3) Systematically evaluate the variations of the thermodynamic preconditions for the shallow-to-deep convection transition among different climate regimes as represented by the six sites of the U.S. Department of Energy's (DOE) Atmospheric Radiation Measurement (ARM) program (Ackerman and Stokes 2003; Stokes and Schwartz 1994), with a focus on the influence of the surface conditions and of entrainment in the ABL, the lower, middle, and upper free troposphere.

Previous studies have shown that the entraining buoyancy calculation is influenced by different factors. One of the most important parameters is the fractional entrainment rate, which is related to many factors of the environment and parcel itself, such as parcel vertical velocity (Neggers et al. 2002), distance to cloud edge (Tian and Kuang 2016), convective area (Simpson and Wiggert 1969), convection proximity (Feng et al. 2015), altitude (Siebesma et al. 2003), ABL height (Siebesma et al. 2007; Soares et al. 2004), relative humidity (Bechtold et al. 2008), low-level CAPE and CIN (Cohen 2000), and buoyancy (Chikira and Sugiyama 2010; Lin 1999). For simplicity, this study only used two entrainment schemes: one is the constant fractional entrainment rate (Const) scheme, and the other is the deep inflow A entrainment (DIA) scheme shown by Holloway and Neelin (2009) and Schiro et al. (2016) to represent buoyancy profiles that are consistent with deep convection. The DIA scheme assumes that the entrainment rate is inversely proportional to altitude. Comparison between these two schemes can give us some qualitative understanding of the contributions from different vertical layers.

The data used in this study are introduced in section 2. The methods for classifying convective regimes and partitioning parcel buoyancy are described in section 3. Section 4 shows how buoyancy components differ between days with only shallow convection and those with

TABLE 1. Summary of sites, seasons, and datasets.

Site	Location	Surface altitude (m)	Time span	Seasons	Radiosonde time (LST)	Precipitation	Cloud radar
SGP	36.61°N, 97.49°W	320	2001–16	Warm: Apr–Sep (Zhang and Klein 2010)	1130	ABRFC	MMCR KAZR
NIM	13.48°N, 2.17°E	205	2006	Monsoon: May–Sep (Kollias et al. 2009)	1030 or 1130	Gauge	WACR-ARSCL
MAO	3.21°S, 60.60°W	50	2014–15	Wet: Jan–May Dry: Jun–Sep Dry-to-wet transition: Oct–Dec (Zhuang et al. 2017)	0730	SIPAM	
TWP1	2.06°S, 147.43°E	4	2001–10	All year	0930	ARMBE	MMCR
TWP2	0.52°S, 166.92°E	4	2003–10	All year	1030		
TWP3	12.42°S, 130.89°E	30	2002–10	Wet: Jan–Apr and Oct–Dec (Frederick and Schumacher 2008)	0830		

shallow-to-deep convection transition at different sites and how entrainment schemes affect this distinction. The main conclusions and a brief discussion as to the limitations and implications of our results are provided in section 5.

2. Data

a. *Geographic and climate regimes represented in this study*

Liu and Zipser (2015) showed that the deepest convective precipitation systems occur most commonly over tropical lands (e.g., Amazon, central Africa), the west Pacific, the U.S. Great Plains, and Argentina. We chose six ARM sites to cover most of these areas: one subtropical site located in the U.S. Southern Great Plains (SGP); two tropical land sites, one in Niamey, Niger (NIM), located in west-central Africa, and the other in Manacapuru, Brazil (MAO), located in the central Amazon; three sites located in the tropical west Pacific (TWP), including Manus Island, Papua New Guinea (TWP1), Nauru (TWP2), and Darwin, Australia (TWP3). SGP, NIM, and TWP3 all experience annually a dry period and a monsoonal wet period. As characteristics of convection can vary seasonally and there are very few deep convective cases during the dry season, we only use their wet seasons with sufficient deep convective cases: April–September for SGP (SGP-W), May–September for NIM (NIM-W), and October–April for TWP3 (TWP3-W). Although there are also relatively dry and wet periods at MAO, the dry season still has ample convective activity and total precipitation; convection characteristics were also shown to vary seasonally (e.g., Machado et al. 2004; Petersen et al. 2002; Zhuang et al. 2017). The wet-to-dry transition at MAO is marked by the decrease of the wet-season type of convection and total precipitation as the rainy area migrates northward, while the dry-to-wet transition season tends to develop the most intense convection. Many previous studies thus treat the dry-to-wet transition season separately from the wet and dry seasons but not for the wet-to-dry transition. Following Zhuang et al. (2017), we analyzed convection separately for three seasons at MAO: the wet season during January–May (MAO-W), dry season during June–September (MAO-D), and dry-to-wet transition season during October–December (MAO-T). TWP1 and TWP2 are two island-based sites next to open ocean; their difference is that TWP1 site is located in the heart of the western Pacific warm pool with frequent deep convection year-round, while TWP2 is in a transition region, and its convection activity is related to the phase of El Niño–Southern Oscillation (Mather and McFarlane 2009). Therefore, season subsetting was not applied to these two oceanic sites, and data in all months were used. Table 1 lists information on the sites, corresponding seasons, and referenced literature.

b. *Sounding profiles*

Only sounding profiles launched after sunrise and before noon are used in this study, as soundings of this time period best represent the preconditions of daytime convection, which are mostly linked to local diurnal forcing. Table 1 also lists launch times for radiosondes at all sites as local standard time (LST) in Table 1. Dry-bulb temperature T, dewpoint temperature T_d, and atmospheric pressure p were used to calculate mixing ratio r, specific humidity q, and buoyancy b. How buoyancy was calculated is discussed in section 3. The data used are available online (at https://www.arm.gov/capabilities/instruments/sonde).

c. *Precipitation*

The precipitation of the Arkansas–Red Basin River Forecast Center (ABRFC) is an hourly gridded precipitation product. It was created as a combination of WSR-88D precipitation estimates and rain gauge reports

(Breidenbach et al. 1998; Fulton et al. 1998). These data are available online (at https://www.arm.gov/capabilities/vaps/abrfc). Spatially averaged data over a 100-km grid box centered at SGP were used here. Precipitation derived using Sistema de Proteção da Amazônia (SIPAM) S-band radar reflectivity with Tokay and Short reflectivity–rain rate (Z–R) relation (Tokay and Short 1996) at 2.5-km altitude and 100-km gridbox mean were used for the MAO site (Zhuang et al. 2017). The reflectivity data are available online (at http://iop.archive.arm.gov/arm-iop/). The ARM best estimate (ARMBE) data product contains a best estimate of several cloud, radiation, and atmospheric quantities, which is generally used to evaluate global climate models. Precipitation data from this product were used here for sites TWP1, TWP2, and TWP3. These data are available online (at https://www.arm.gov/capabilities/vaps/armbe). Rain gauge data were used for the NIM site as no other product is available. The gauge data are available online (at https://www.arm.gov/capabilities/instruments/rain). Precipitation data listed above were processed to hourly mean rain rate and used to determine deep and shallow convection days. The method for the classification is discussed in section 3.

d. Cloud radar reflectivity

The millimeter-wavelength cloud radar (MMCR) (Moran et al. 1998) operates at a frequency of 35 GHz and is designed to map the vertical distribution of cloud directly above the radar. This radar is available at SGP (2001–11), TWP1, TWP2, and TWP3. The Ka-band ARM zenith radar (KAZR) replaced the MMCR and provides higher spatial and temporal resolution at SGP after 2011. For NIM and MAO, the vertical profiles of cloud mask were retrieved from the W-band ARM cloud radar active remote sensing of clouds (WACR-ARSCL) data (available at https://www.arm.gov/data/vaps/wacrarscl/arsclwacr1kollias). This product is derived from combined observations from the 95-GHz WACR, micropulse lidar (MPL), and ceilometer using the new WACR-ARSCL value-added product (VAP) algorithm (Kollias et al. 2007). Cloud fraction, defined as temporally fractional coverage every 12 min, was calculated from the MMCR–KAZR hydrometeor-mask and the WACR-ARSCL cloud-mask data at each level for further analysis. The cloud fraction data in addition to precipitation data were used to help identify shallow convection days.

3. Methods

a. Classification of convective regimes

We adopt a method similar to that used by Zhang and Klein (2010), where a DC day is defined as a day with maximum hourly precipitation that 1) exceeds 1 mm h^{-1}, 2) occurs between 1100 and 1800 LST, and 3) is at least twice as large as maximum hourly precipitation between 0000 and 0700 LST. An SC day is defined as a day that must satisfy one of the following two sets of criteria: 1) maximum hourly precipitation is below 0.1 mm h^{-1} and shallow clouds (cloud base $<$ 3 km, cloud top $<$ 6 km) can be seen by cloud radar for at least 0.5 h or 2) maximum hourly precipitation is above 0.1 mm h^{-1} but below 1 mm h^{-1} and no significant low clouds (cloud base $<$ 3 km) can be seen by cloud radar.

Figure 1 shows the diurnal cycle of composite temporal cloud fraction (CF) and 12-min average rain rate for SC and DC cases classified by the above method. Significant CF and precipitation differences between DC and SC can be seen at all sites, suggesting the case classification results should be reliable enough for the composite analysis to show thermodynamic condition differences between the two types of cases. Note that the composite diurnal cycle at NIM-W is more irregular than those at other sites because of fewer available samples of either case; thus, one should be cautious with the interpretation of the composite result at NIM-W in the following sections. There are also some regional and seasonal differences seen in Fig. 1. For SC cases, land sites SGP-W and MAO and coastal site TWP3-W show larger vertical extension of shallow clouds than oceanic sites TWP1 and TWP2; shallow clouds at MAO appear to form later and have shorter lifetimes than at SGP-W and TWP, and the wet season appears to have larger CF than the dry and transition seasons; shallow clouds in TWP1 and TWP2 have lower cloud-top heights, though they can exist almost all day. For DC cases, land sites generally have larger low-level CF than oceanic sites (SGP-W $\approx$ NIM-W $\approx$ MAO-W $>$ MAO-D $\approx$ MAO-T $\approx$ TWP3-W $>$ TWP1 $>$ TWP2); most sites reach the maximum low-level CF in the early afternoon; however, SGP-W and TWP3 have a peak precipitation rate 3–5 h later than MAO, TWP1, and TWP2.

b. Parcel buoyancy calculation and decomposition

In our simple entraining parcel model, we assume that a rising parcel originating from the surface goes through three processes from altitude z to $z + \Delta z$: the parcel ascends without interacting with the environment, then ambient air is entrained into the parcel, and condensates are precipitated out of the parcel.

The first process in which the parcel ascends without interacting with the environment can be regarded as a process that conserves the parcel system entropy, with the parcel system including dry air, water vapor, liquid water, and ice. An accurate expression of the specific entropy of such a system is (Hauf and Holler 1987)

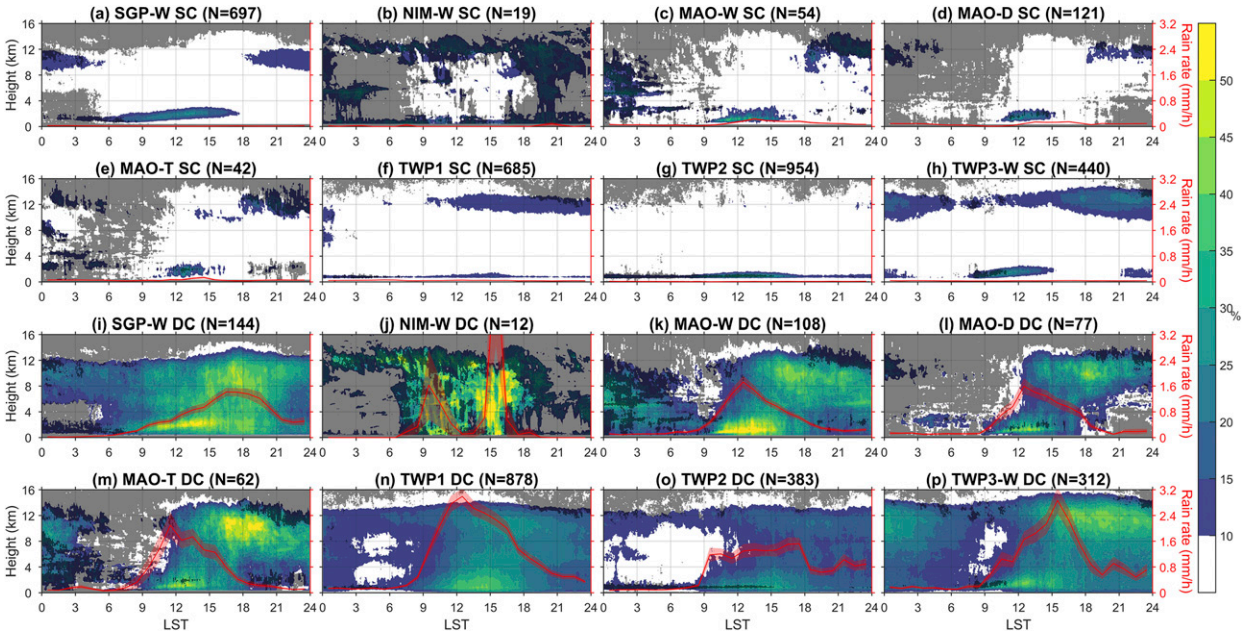

FIG. 1. Composite diurnal cycle of CF (color shades) and precipitation (red lines) for (a)–(h) SC and (i)–(p) DC cases. The black shading represents where the composite CF of DC cases is not significantly larger than that of SC cases as determined by the Student's *t* test at the 0.05 level. Sample number *N* is indicated in the title of each panel.

$$s = s_d(1-q_t) + s_l q_t + \frac{l_{lv}+a_{lv}}{T}q_v - \frac{l_{il}+a_{il}}{T}q_i, \qquad (1)$$

where $s_d = c_{pd}\ln(T/T_0) - R_d\ln(p_d/p_0) + s_d(0)$ is the partial entropy of dry air, $s_l = c_l\ln(T/T_0) + s_l(0)$ is the partial entropy of liquid water, $l_{lv} = l_{lv}(T_0) - (c_l - c_{pv})(T - T_0)$ is the latent heat of condensation/vaporization, $l_{il} = l_{il}(T_0) - (c_i - c_l)(T - T_0)$ is the latent heat of freezing/fusion, $a_{lv} = R_v T\ln(e_{sl}/e)$ and $a_{il} = R_v T\ln(e_{si}/e_{sl})$ are the affinities, and $p_d = [R_d/(R_d + R_v r_v)]p$ is the partial pressure of dry air (meanings of other variables and constants can be found in appendix A). If the parcel is assumed to be ice free and in an equilibrium state, the conservation of system entropy is equal to the conservation of equivalent potential temperature θ_e (Hauf and Holler 1987). For simplicity, the equilibrium state is also assumed in this study, which means the parcel always remains saturated if possible, but ice process is included. This process that conserves the system entropy will be referred to as a moist isentropic process to differentiate it from the isentropic process in meteorology that generally means a dry adiabatic process. To calculate parcel temperature at $z + \Delta z$, we use a Newton–Raphson technique, which can converge to high accuracy in several steps, and a traditional weighting technique (Tao et al. 1989) is used to determine the proportion between liquid and ice water mixing ratios when an air parcel is saturated.

For the entrainment process, the parcel mixes with ambient air isobarically following $A_{k+1} = (A_k + X\tilde{A}_k)/(1+X)$, where X is the fractional entrainment rate; A is a conserved variable of the parcel during entrainment, which is total water mixing ratio r_{tp} and enthalpy $h = (c_{pd} + c_{pv}r_{vp} + c_l r_{lp} + c_i r_{ip})T_p$; $\tilde{A}$ is the environmental value [water vapor mixing ratio r_{ve} and enthalpy $h = (c_{pd} + c_{pv}r_{ve})T_e$]; and k denotes the altitude level. In this study, three entrainment schemes are used: no entrainment ($X = 0$), constant entrainment ($X = \text{const} \times \Delta z$), and DIA entrainment (Holloway and Neelin 2009; Schiro et al. 2016). For the DIA scheme, fractional entrainment rate follows the relationship $X(z) = c_\epsilon \Delta z/z$, where $c_\epsilon = 0.4$, z is the height above the surface, and the vertical step $\Delta z = 10$ m. For the Const scheme, the constant in the fractional entrainment rate is set to $10^{-4}\,\text{m}^{-1}$, which results in a constant entrainment rate equal to that of the DIA scheme at 4 km.

During the precipitation process, condensates formed from the previous two processes will fall out. For simplicity, only two extreme scenarios are considered: zero-condensate loading (all condensates fall out) and full-condensate loading (all condensates remain in the parcel).

A buoyancy decomposition method was used to partition total buoyancy into several components based on the above three main processes. A detailed derivation of the method is provided in appendix B. The decomposition result is as follows:

TABLE 2. Summary of decomposed buoyancy terms.

Process		Symbol	Representation	Expression of $\frac{db_{()}}{dz}$
Profile related		b_t	Temperature profile	$-g\frac{T_p}{T_e}\frac{d\ln T_e}{dz}$
		b_r	Humidity profile	$-g(\varepsilon^{-1}-1)\frac{dr_{ve}}{dz}$
Moist isentropic ascent		b_{S-a}	Dry adiabatic cooling	$g\frac{T_p}{T_e}\frac{R_d}{c_{pd}}\frac{d\ln p}{dz}$
		b_{S-w}	Heat exchange among different water phases	$g\frac{T_p}{T_e}\left(\frac{R_m}{c_{pml}}-\frac{R_d}{c_{pd}}\right)\frac{d\ln p}{dz}$
		b_{S-c}	Condensation/vaporization	$g\left(\varepsilon^{-1}-\frac{l_{lv}}{c_{pml}T_e}\right)\left(\frac{dr_{vp}}{dz}\right)_S$
		b_{S-f}	Freezing/fusion	$g\frac{l_{il}}{c_{pml}T_e}\left(\frac{dr_{ip}}{dz}\right)_S$
Entrainment	Mixing without phase change of water	b_{E1-m}	Temperature mixing	$\frac{g}{T_e}\frac{\chi}{1+\chi}\frac{T_e-T_p}{\Delta z}$
		b_{E1-w}	Heat exchange among different water phases	$\frac{g}{T_e}\frac{(c_{pml}/c'_{pml}-1)T_p-\chi(c_{pm}/c'_{pml}-1)T_e}{(1+\chi)\Delta z}$
		b_{E1-v}	Change of water vapor mixing ratio	$g(\varepsilon^{-1}-1)\frac{X}{1+X}\frac{r_{ve}-r_{vp}}{\Delta z}$
		b_{E1-li}	Change of condensate mixing ratio	$g\frac{X}{1+X}\frac{r_{lp}+r_{ip}}{\Delta z}$
	Phase change of water	b_{E2-c}	Condensation/vaporization	$g\left(\varepsilon^{-1}-\frac{l_{lv}}{c_{pml}T_e}\right)\left(\frac{dr_{vp}}{dz}\right)_{E2}$
		b_{E2-f}	Freezing/fusion	$\frac{g}{T_e}\frac{l_{il}}{c_{pml}}\left(\frac{dr_{ip}}{dz}\right)_{E2}$
Precipitation		b_P	Condensate loss	$-g\left[\left(\frac{dr_{lp}}{dz}\right)_P+\left(\frac{dr_{ip}}{dz}\right)_P\right]$
Error term		b_ε	Total buoyancy minus the sum of all terms above	—

$$b = b_t + b_r + b_{S-a} + b_{S-w} + b_{S-c} + b_{S-f} + b_{E1-m} + b_{E1-w} + b_{E1-v} + b_{E1-li} + b_{E2-c} + b_{E2-f} + b_P + b_\varepsilon. \quad (2)$$

All the above decomposed buoyancy terms are summarized in Table 2. Temperature and dewpoint temperature profiles were interpolated with a 10-m interval before going into the buoyancy calculation. Buoyancy profiles for all sites were calculated with surface parcels (i.e., surface temperature and specific humidity are used as initial conditions of the parcel). Figure 2 shows an example of a buoyancy decomposition result using a sounding profile at 0730 LST 7 January 2014 at MAO. The first row in Fig. 2 shows buoyancy components related to environmental profiles and the isentropic process; the second row shows buoyancy components related to the entrainment process; the last row shows the sum of the first row, the sum of the second row, the buoyancy component related to precipitation process, total buoyancy, and the error term in the decomposition. From the magnitude of the buoyancy components, we can identify the three largest components related to the main processes of parcel theory: b_t, b_{S-a}, and b_{S-c}, which represent the environmental temperature profile (contrast between initial temperature and temperature at parcel level), dry adiabatic ascent, and latent heat release from condensation, respectively. The values of b_{E1-w} and b_{E2-f} are similar orders of magnitude as the error term b_ε, suggesting their contributions can be neglected.

4. Buoyancy contrast between SC and DC cases

In this section, we focus on analyzing the composite profiles of different buoyancy components for both DC and SC cases or for their differences. Profiles with zero-condensate loading ($b_P \geq 0$) and full-condensate loading ($b_P = 0$) schemes are both plotted for all figures to show the influence of condensate loading, as we assume that the most realistic profile should be somewhere in between.

a. Total buoyancy

Figure 3 shows the composite buoyancy profiles for SC and DC cases calculated without entrainment. DC and SC cases only show significant positive buoyancy

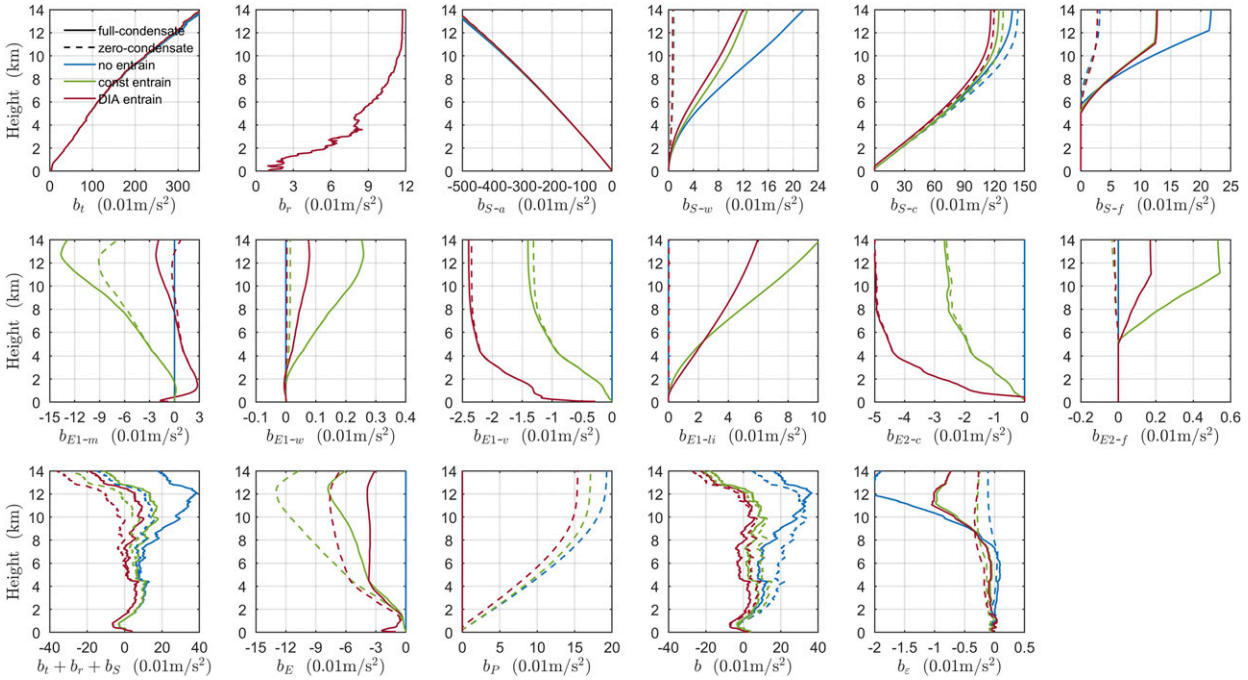

FIG. 2. An example of buoyancy decomposition using a sounding profile at 0730 LST 7 Jan 2014 at MAO. Detailed descriptions of all the buoyancy components are listed in Table 2.

differences at SGP-W and TWP3-W; at MAO-T, the difference even becomes negative, which is unrealistic since we expect larger buoyancy for DC cases; at other sites, the buoyancy profiles do not have significant differences between DC and SC cases for most levels. A reasonable explanation is that the traditional buoyancy calculated without entrainment could largely depend on surface thermodynamic condition, and this surface condition may not differ between DC and SC cases at all sites. Although a higher surface humidity generally occurs during DC days in drier areas or seasons and contributes to a larger buoyancy, surface temperature for DC cases could be similar to or even lower than SC cases as a result of a greater cloud fraction and less shortwave radiation reaching the surface.

In addition, buoyancy with the zero-condensate loading scheme is significantly higher than that with the full-condensate loading scheme at altitudes below ~11 km as a result of less condensate mass inside the parcel; above that level, the relation reverses as more condensates in the full-condensate loading scheme lead to more ice formation and result in more latent heat release. Although buoyancy profiles are very different for these two condensate loading schemes, differences between DC and SC cases are very similar for both schemes.

To incorporate more influences from the environment above the surface and better differentiate the buoyancy profiles of the DC and SC cases, two entrainment schemes (Const and DIA) are added into the buoyancy calculation. The formulas shown in section 3 indicate that the Const scheme has more entrainment at high altitudes than the DIA scheme because of the inverse altitude dependence of the latter. Figure 4 shows the composite buoyancy profile difference between DC and SC cases ($b_{DC} - b_{SC}$) for three entrainment scenarios: no entrainment, Const entrainment, and DIA entrainment. At SGP-W, entrainment increases $b_{DC} - b_{SC}$ very slightly below ~8 km. Likewise, at NIM-W, entrainment shows little effect on increasing $b_{DC} - b_{SC}$. At MAO, $b_{DC} - b_{SC}$ increases very significantly with entrainment schemes at most levels, especially during drier seasons (MAO-D and MAO-T); the DIA scheme has a $b_{DC} - b_{SC}$ nearly twice as large as that with the Const scheme at MAO-W and MAO-D, and only the DIA scheme shows significantly positive $b_{DC} - b_{SC}$ at MAO-T. At TWP1, TWP2, and TWP3-W, DIA scheme leads to larger $b_{DC} - b_{SC}$ in the lower free troposphere than the Const scheme, but when the parcel goes into the middle and upper troposphere, this contrast between the DIA and Const schemes is not as significant as that at MAO. This difference indicates that the lower-tropospheric entrainment could play a more important role in the Amazon than in the tropical ocean. The reason for the DIA scheme's larger impact on increasing buoyancy difference is discussed in some following analyses.

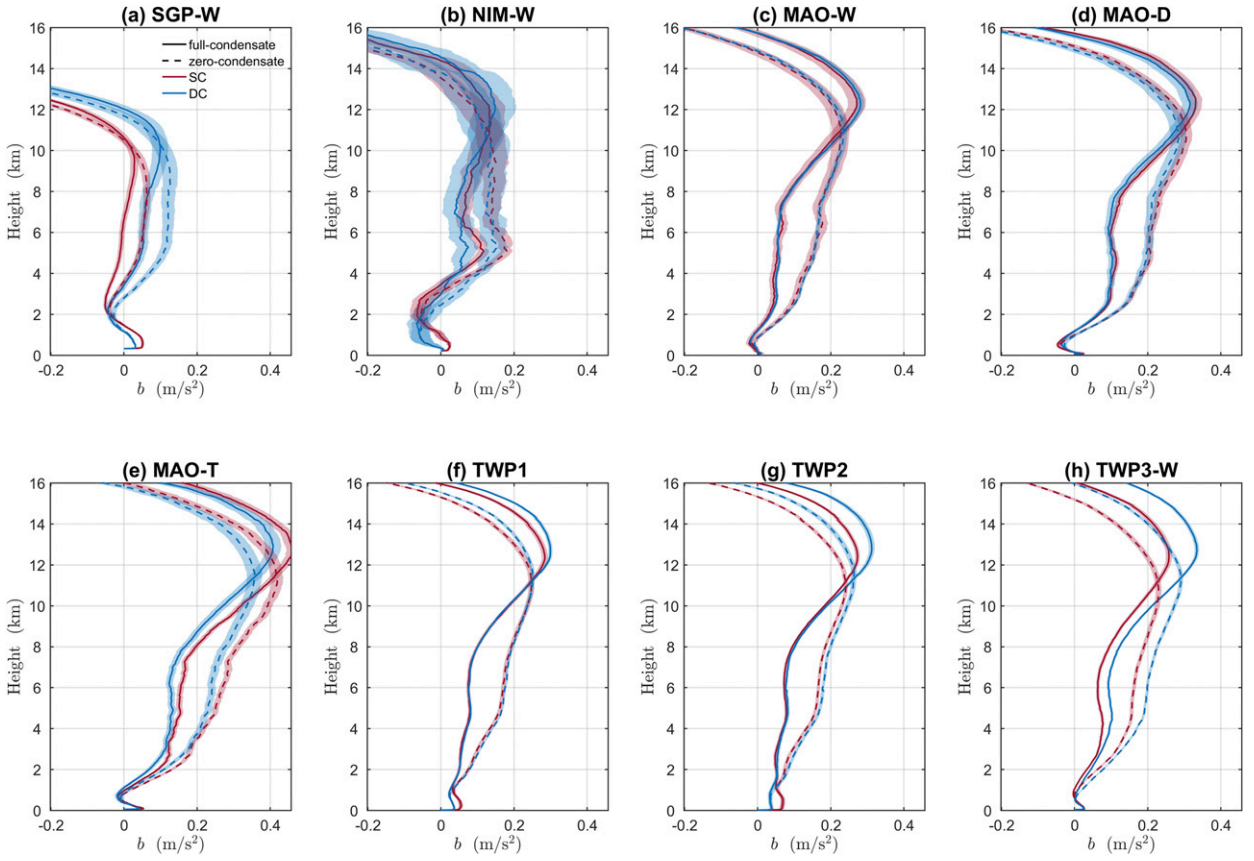

FIG. 3. Composite profiles for the total buoyancy b without entrainment for the SC and DC cases at all sites. Shading represents plus and minus one standard error.

b. *Temperature profile and b_t*

By using the definition of db_t/dz in appendix B and integrating it from surface z_0 to altitude z, we have $b_t = \int_{z_0}^{z}(db_t/dz)\,dz \approx -\int_{z_0}^{z}(d\ln T_e/dz)\,dz = g\ln[T_e(z_0)/T_e(z)]$. This means the temperature profile term b_t is almost totally determined by the temperature profile $T_e(z)$ and the initial temperature of the parcel [surface temperature $T_e(z_0)$]. Figure 5 shows negative b_t difference $(b_t)_{\mathrm{DC}} - (b_t)_{\mathrm{SC}}$ at most levels for all sites except MAO-W. This is mostly caused by larger surface temperature in SC days due to less cloud cover and more solar heating on the surface, since $b_t(z) \approx g\ln[T_e(z_0)/T_e(z)]$ at any level z is affected by the surface temperature $T_e(z_0)$. This term's high dependence on initial temperature well explains, using traditional method for buoyancy calculation (surface-based parcel, no entrainment), why the buoyancy for SC cases could be close to or larger than that for DC cases (Fig. 3). At MAO (Figs. 5c–e), since the sounding time is the earliest (~0730 LST) among all sites, it does not contribute to a negative b_t difference as large as at other sites.

c. *Condensation and b_c*

The condensation term in moist isentropic ascent b_{S-c} is another buoyancy component with the largest order of magnitude. In this part, we will compare $b_c = b_{S-c} + b_{E2-c}$ between DC and SC cases and see how the contribution from latent heat of condensation varies. We chose to study the total condensation term b_c instead of b_{S-c} considering that they are both related to the latent heat release from condensation, though they occur in two different processes (moist isentropic ascent and isobaric entrainment). In Fig. 6, we can see that the positive $(b_c)_{\mathrm{DC}} - (b_c)_{\mathrm{SC}}$ without entrainment (black line) is not large enough to compensate for the negative $(b_t)_{\mathrm{DC}} - (b_t)_{\mathrm{SC}}$ at MAO, TWP1, and TWP2 (Figs. 5c–g). This balance between the temperature profile term b_t and condensation term b_c mostly explains why buoyancy for DC could be smaller than that for SC at these sites. After adding entrainment process into the buoyancy calculation, $(b_c)_{\mathrm{DC}} - (b_c)_{\mathrm{SC}}$ becomes larger for MAO and three TWP sites; for MAO-D and MAO-T, the DIA scheme increases $(b_c)_{\mathrm{DC}} - (b_c)_{\mathrm{SC}}$ much more significantly

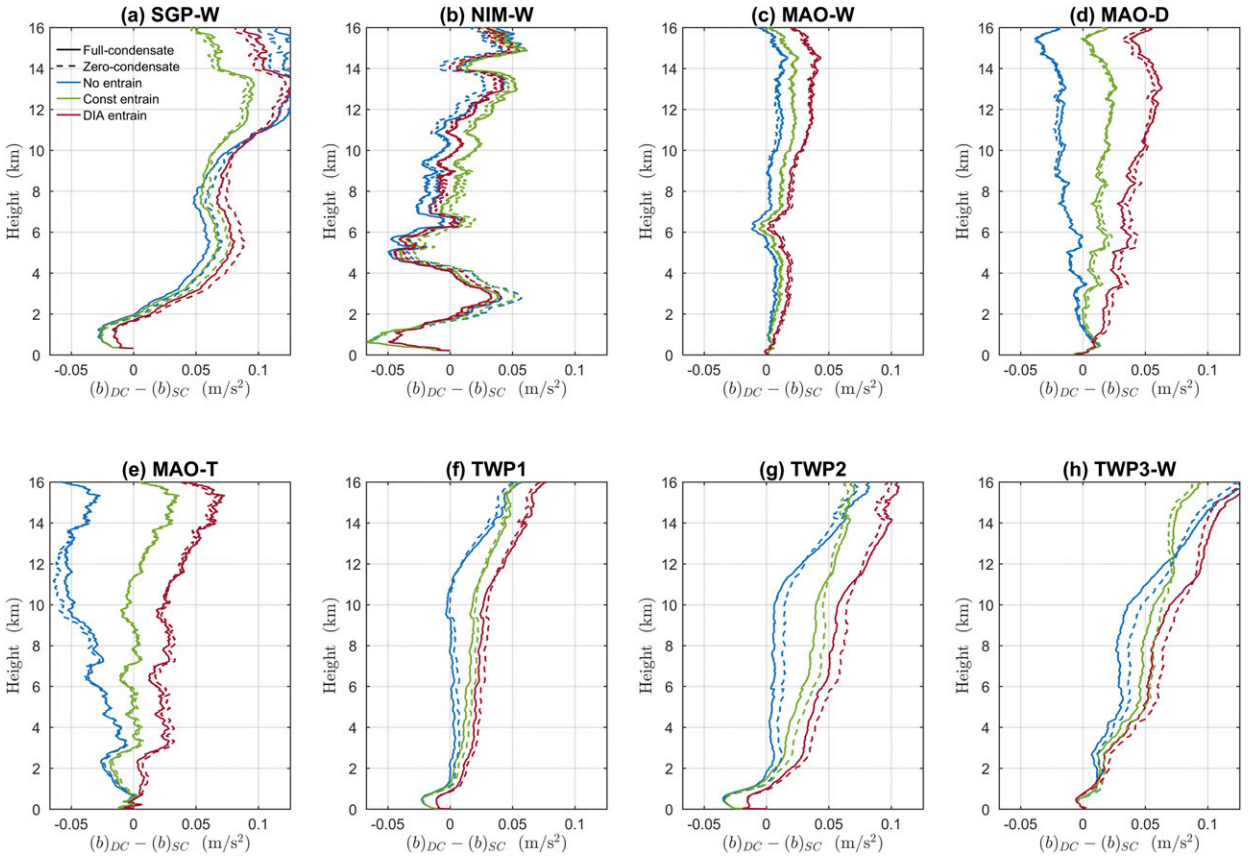

FIG. 4. Differences of composite profiles for the total buoyancy b between the DC and SC cases for three entrainment schemes at all sites.

than the Const scheme. This is because low-level entrainment can significantly limit the formation of the condensates for SC cases in a drier environment (dry and transition seasons) in the Amazon. This is also the main reason for the greater increase of $(b_c)_{\mathrm{DC}} - (b_c)_{\mathrm{SC}}$ between the DIA and Const schemes at MAO than at TWP. However, entrainment's effect on increasing $(b_c)_{\mathrm{DC}} - (b_c)_{\mathrm{SC}}$ at SGP-W is rather small; at NIM-W, the DIA scheme even decreases $(b_c)_{\mathrm{DC}} - (b_c)_{\mathrm{SC}}$.

As b_c mainly represents a parcel's ability to transform water vapor to buoyancy via condensation, it is mainly determined by the humidity conditions both at the surface and in the atmosphere above (if considering entrainment). As discussed before, b_t is strongly affected by surface heating, and its difference between DC and SC cases is generally negative. As this condensation term b_c does not contains b_t as total buoyancy b does, b_c generally shows a more significant difference between the DC and SC cases than does the total buoyancy b. CAPE or the integral of buoyancy is often used to assess the atmospheric instability. In Fig. 7, we explore whether $\int_{z_0}^{z_t} b_c \, dz$ could better represent the thermodynamic precondition for the shallow-to-deep convection transition than CAPE and $\int_{z_0}^{z_t} b \, dz$. We compared these three variables calculated from different entrainment schemes for the SC and DC cases at all sites. CAPE was calculated as the integral of buoyancy between the level of free convection (LFC) and the limit of convection (LOC). For the integral, the lower-limit z_0 is the surface altitude, and the upper limit z_t is arbitrarily set to 12 km here. The central rectangle in each box spans from the first quartile to the third quartile of the sample, which corresponds to 50% of the sample. The Student's t test was also performed to show if the difference between the DC and SC cases is significant. The test results are shown as the colors of x-axis labels in Fig. 7. Blue labels represent sites where the DC value is significantly larger than SC, while red labels mean SC is larger than DC; for blue and red labels, bold (plain) font means the difference is significant at the 0.01 (0.05) level; black labels indicate the difference is insignificant. We can see that CAPE and $\int_{z_0}^{z_t} b \, dz$ differ very little between the SC and DC cases at nearly all sites if entrainment is not included in buoyancy calculation (Figs. 7a,d), as there are big overlaps for the central rectangles; only SGP-W and TWP3-W show significantly larger value for DC cases.

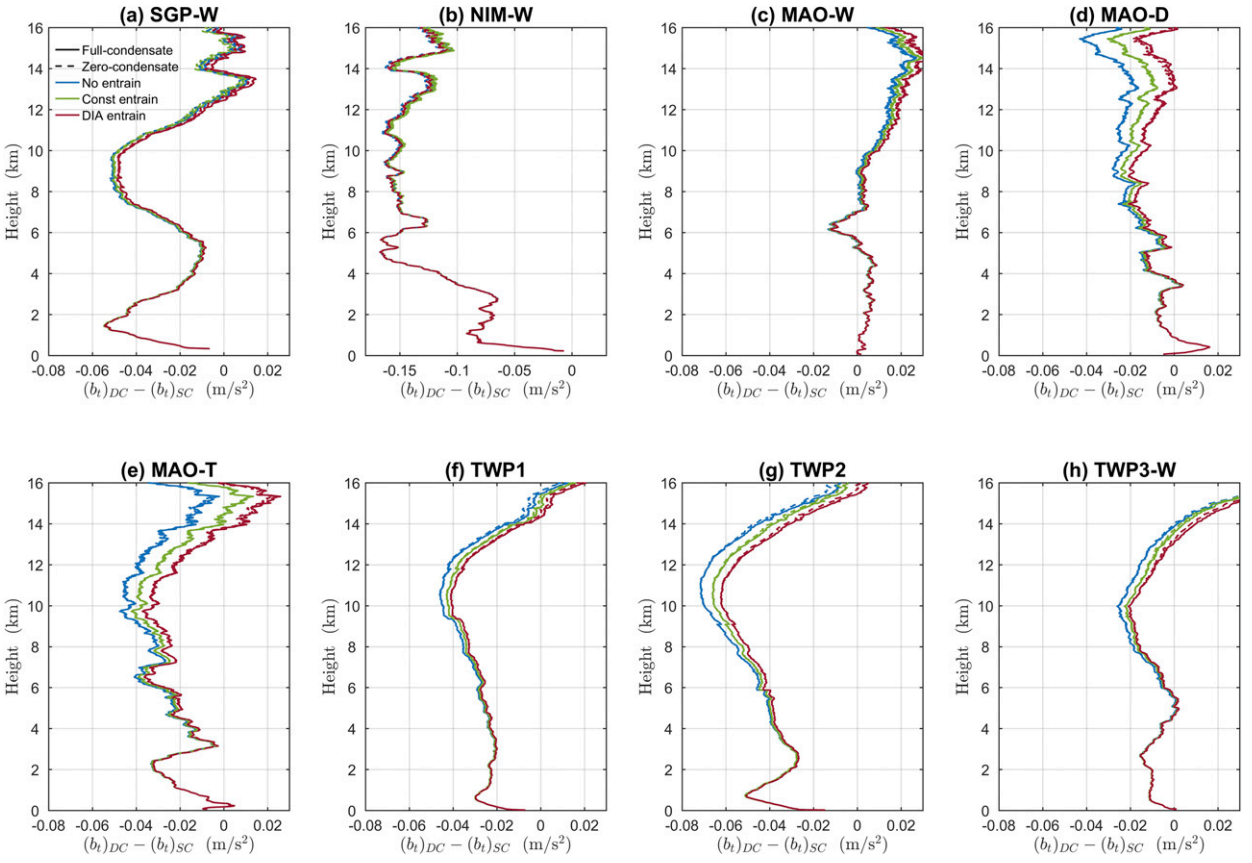

FIG. 5. As in Fig. 4, but for the temperature profile term b_t.

As indicated by Figs. 7b and 7e, adding the Const entrainment makes the difference of CAPE and $\int_{z_0}^{z_t} b\,dz$ significant for SGP-W and TWP; the DIA entrainment further makes the difference statistically significant at all sites except NIM-W (Figs. 7c,f). On the other hand, $\int_{z_0}^{z_t} b_c\,dz$ between the DC and SC cases is significant even without entrainment at all sites except MAO (Fig. 7g); by comparison, $\int_{z_0}^{z_t} b_c\,dz$ shows a larger contrast between the DC and SC cases than CAPE or $\int_{z_0}^{z_t} b\,dz$ with either entrainment scheme (Figs. 7h,i). The distinction of $\int_{z_0}^{z_t} b_c\,dz$ between the DC and SC cases is the clearest with the DIA scheme (Fig. 7i). Overall, Fig. 7 suggests that the integral of the condensation term $\int_{z_0}^{z_t} b_c\,dz$ is a better index to assess a precondition for the shallow-to-deep convection transition, mostly because it reflects the parcel's most important heating source, latent heat release of condensation, and excludes the temperature profile term b_t from the total buoyancy (b_t is too sensitive to the surface insolation and can vary strongly during a diurnal cycle).

d. *Freezing and b_f*

The freezing term $b_f = b_{S-f} + b_{E2-f}$ varies a lot with the choice of condensate loading scheme as demonstrated by the example in Fig. 2. With zero-condensate loading scheme ($b_P \geq 0$), b_f becomes small enough to be neglected; with full-condensate loading scheme ($b_P = 0$), although b_f difference between the DC and SC cases becomes larger, its value is still about one order of magnitude smaller than the b_c difference. Although b_f is not a large contributor to buoyancy difference between the DC and SC cases under our assumption for freezing, its increase implies more ice formation and deep convection potentially with more lightning activity. By exploring how entrainment influence b_f at these six sites, we can potentially provide a thermodynamic explanation for more ice and more frequent occurrence of lightning associated with deep convection over subtropical continents than over tropical oceans observed by satellites (e.g., Liu and Zipser 2015; Zipser et al. 2006).

As described in section 3b, the proportion between ice and liquid water condensate is determined by a weighting technique from Tao et al. (1989). Specifically, the proportion of ice condensate linearly changes from 0 to 1 when temperature changes from 0° to −40°C. This assumption of ice condensate's gradual increase with height may lead to underestimation of the contribution

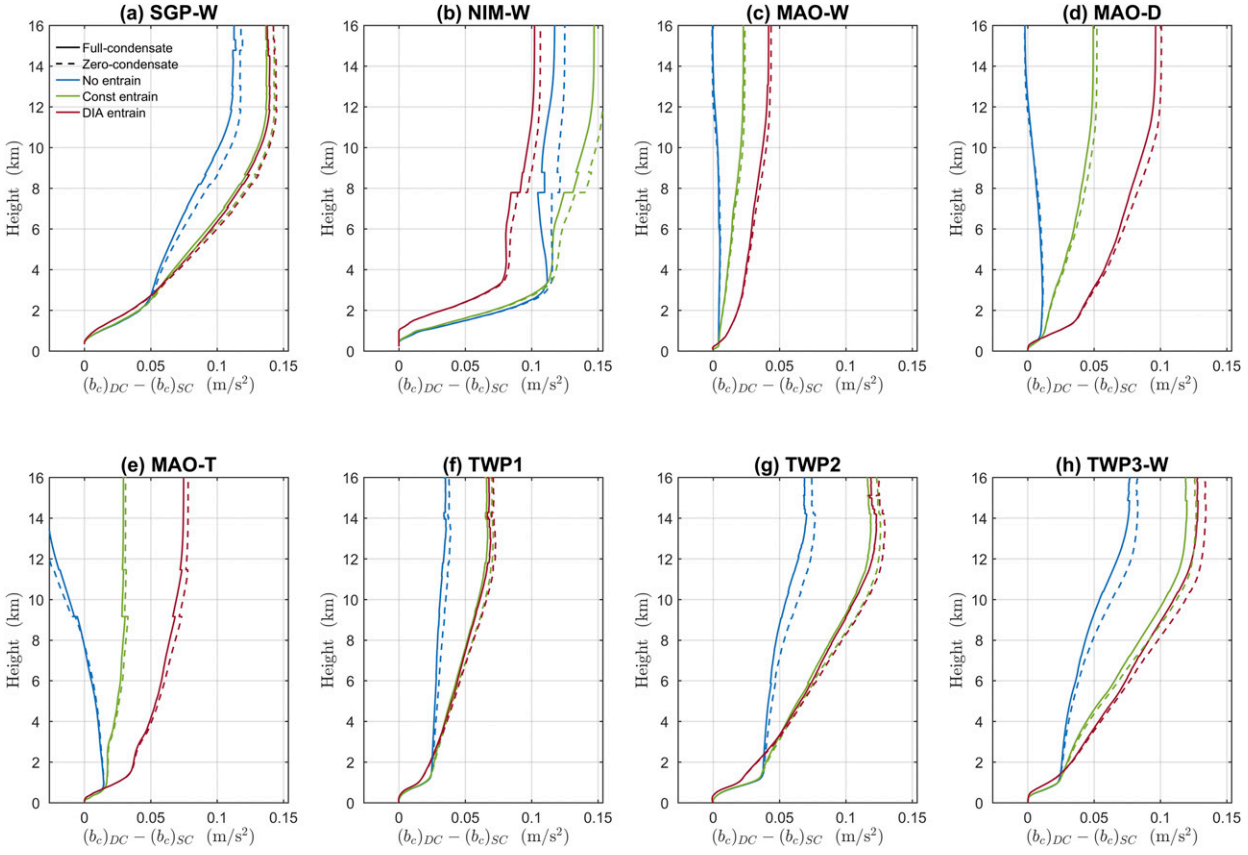

FIG. 6. As in Fig. 4, but for the condensation term b_c.

of the freezing term to the total buoyancy. Schiro et al. (2016) showed a much more significant impact of freezing on increasing buoyancy for convection events using a more extreme freezing scenario, where the proportion of ice condensation changes abruptly from 0 to 1 when the parcel temperature drops below 0°C. This study does not attempt to reach a more precise estimation of b_f since it is affected by more factors like aerosol loading (Altaratz et al. 2014) and thus requires more observational studies. However, as b_f represents the additional latent heat contribution from ice formation, and ice content can be another useful indicator for convection intensity, we thus assess the ratio of $\int_{z_0}^{z_t} b_f \, dz$ to $\int_{z_0}^{z_t} b_c \, dz$ for DC cases to see how ice formation varies with ambient air humidity among all sites from a thermodynamic viewpoint. As described before, z_0 is surface altitude, and z_t is set to be 12 km.

Figure 8 shows the scatterplot between $\int_{z_0}^{z_t} b_f \, dz / \int_{z_0}^{z_t} b_c \, dz$ and precipitable water vapor (PWV) with DIA entrainment scheme for DC cases. Regression lines for all sites in Fig. 8 all show negative correlation between $\int_{z_0}^{z_t} b_f \, dz / \int_{z_0}^{z_t} b_c \, dz$ and PWV for both full- and zero-condensate loading schemes, suggesting a higher ratio of freezing to condensation in a less humid environment. Full-condensate loading shows a larger correlation coefficient and larger contribution from ice process than zero-condensate loading. The coefficient of determination R^2 ranges from 0.59 to 0.84 with full-condensate loading (from 0.52 to 0.64 with zero-condensate loading) for all sites, suggesting a robust correlation. Among all sites, SGP-W and NIM-W show similar regression coefficients k, whereas MAO and three TWP sites show similarly smaller negative coefficients. This result is consistent with and potentially provides a thermodynamic explanation for previous observational studies that show more ice and higher lightning rate associated with deep convection over subtropical continents than over tropical oceans (Liu and Zipser 2015; Zhang et al. 2008; Zipser et al. 2006) and more intense convection during the dry and transition seasons than the wet season over the Amazon (Williams et al. 2002; Zhuang et al. 2017). Notice that the total convective precipitation/buoyancy, mainly contributed by condensation, increases with PWV, as shown previously (Holloway and Neelin 2009; Schiro et al. 2016) over humid tropical land and ocean.

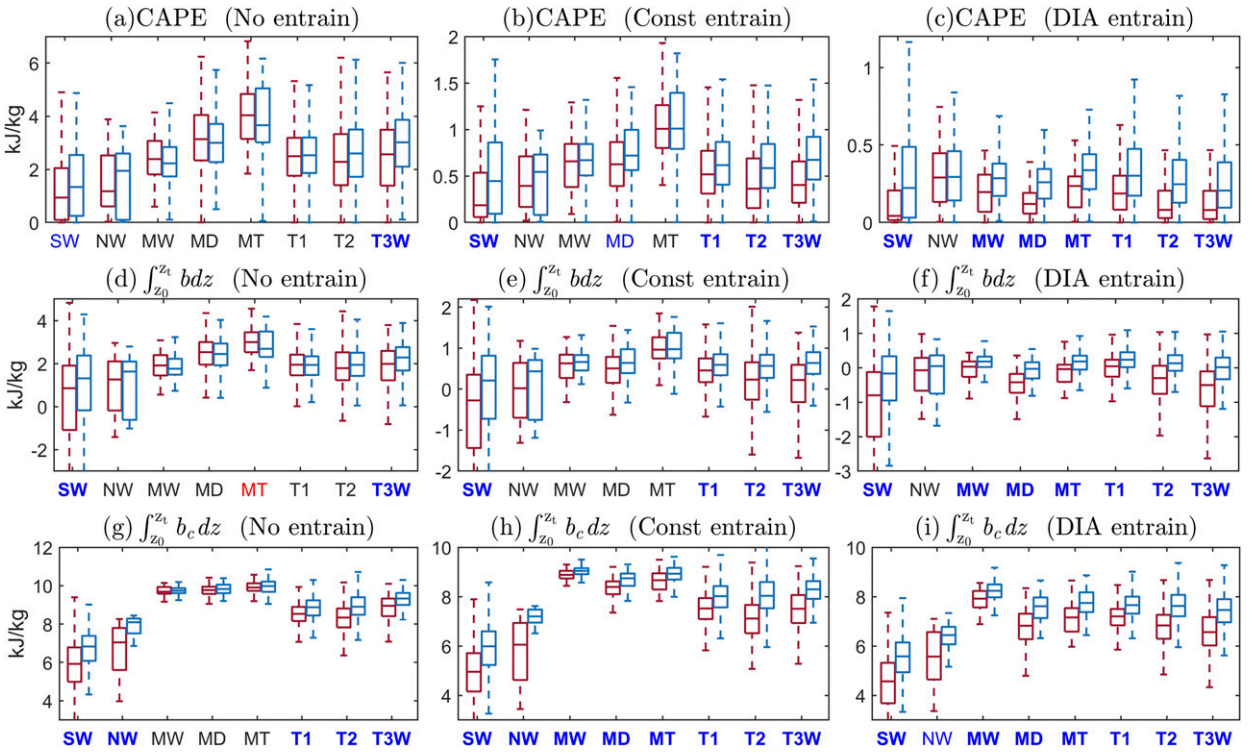

FIG. 7. Box-and-whisker plots of three indices related to the integral of buoyancy for the SC and DC cases (red and blue boxes, respectively) at all sites: (a)–(c) CAPE, (d)–(f) the integral of total buoyancy from z_0 (surface) to z_t (12 km), and (g)–(i) the integral of condensation term b_c from z_0 (surface) to z_t (12 km). Indices are calculated with (a),(d),(g), no entrainment; (b),(e),(h) Const entrainment; and (c),(f),(i) DIA entrainment. Each box spans from the first quartile (Q1) to the third quartile (Q3) of the sample, The median value is the line inside the rectangle. Data points larger than Q3 + 1.5 × (Q3 − Q1) or smaller than Q1 − 1.5 × (Q3 − Q1) are outliers but not shown. The whiskers extend to a furthest value that is not an outlier. The Student's t test is performed for each site in each panel between the DC and SC values. Sites at which the mean DC value is significantly larger than the mean SC value are in blue text on the x axis, sites with an SC value significantly larger than the DC value are in red text, and sites where the DC and SC values are not significantly different is in black text. For red and blue text, if the difference is significant at the 0.01 level, the text is boldface; if the difference is only significant at 0.05 level, plain font is used.

e. Humidity dilution and b_{E1-v}

In the entraining parcel model, direct impacts of entrainment on the parcel include two aspects: temperature mixing and humidity dilution. The change of water vapor mixing ratio in the parcel during the entrainment b_{E1-v} can represent the humidity dilution aspect of entrainment. Besides its direct contribution to total buoyancy, decrease of b_{E1-v} with height also indicates reduction of available water vapor, which can lead to decrease of b_c. Figure 9 shows the composite b_{E1-v} profiles for the SC and DC cases. At SGP-W and three TWP sites, although the DIA scheme (thick lines) causes more water vapor dilution (larger negative b_{E1-v}) because of a larger entrainment rate in the lower troposphere than the Const scheme (thin lines), the b_{E1-v} difference between the DC and SC cases is similar for both entrainment schemes, but for MAO, the difference becomes significantly larger for the DIA scheme. This again explains why the DIA scheme has a greater effect on increasing $b_{DC} - b_{SC}$ through more humidity dilution contrast between the DC and SC cases at lower levels. For the DIA scheme, the SC cases already show significantly more water vapor dilution than the DC case in the ABL (below ~1 km) at MAO, while at SGP-W and three TWP sites, the level where the SC cases pick up most water vapor dilution is the lower free troposphere (~2–5 km). Therefore, for the humidity dilution aspect, the ABL and lower free troposphere make important contributions to the buoyancy difference between the DC and SC cases at MAO. However, at SGP-W and TWP, humidity dilution due to ABL entrainment does not have as important an impact as that of the lower-tropospheric entrainment. Seasonal and geographical differences also exist as suggested in Fig. 9: the dry and transition seasons at MAO (MAO-D and MAO-T) have more significant humidity dilution (larger negative b_{E1-v}) and larger b_{E1-v} contrast between the DC and SC cases than the wet season (MAO-W) because of their

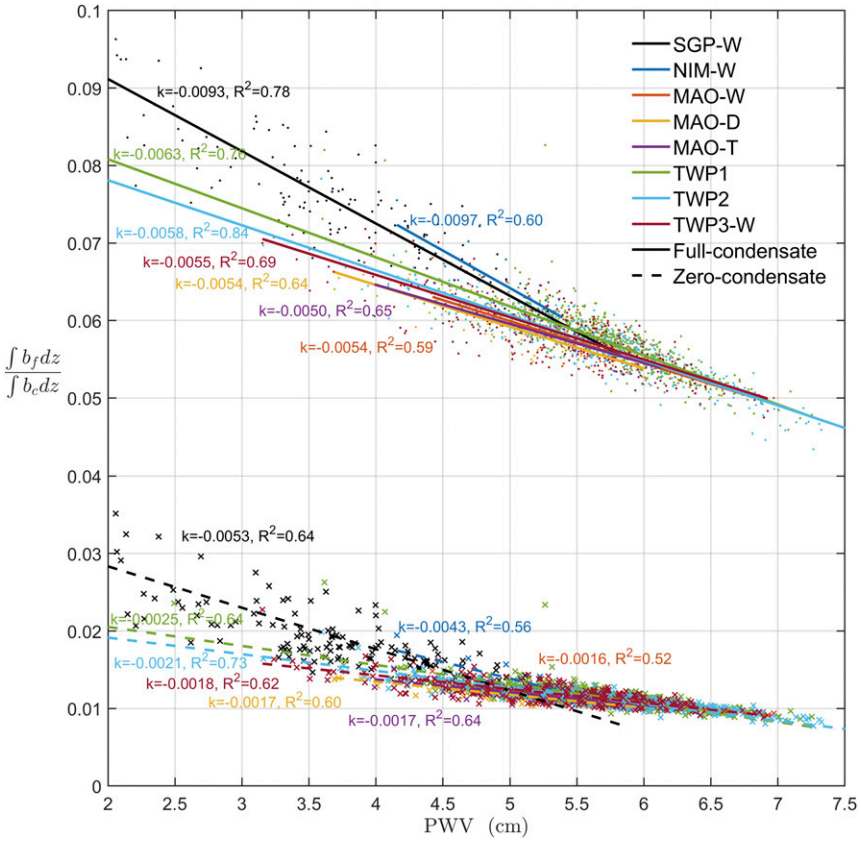

FIG. 8. Scatterplot and regression lines for the ratio of the integral of freezing term to the integral of condensation term $\left(\int_{z_0}^{z_t} b_f\, dz / \int_{z_0}^{z_t} b_c\, dz\right)$ vs PWV for DC cases with the DIA entrainment scheme. (top) Solid lines and dots represent the full-condensate loading scheme; (bottom) dashed lines and × markers represent zero-condensate loading scheme. Each point represents a single sounding profile. The regression coefficient k and the coefficient of determination R^2 for each line are also marked.

relatively drier atmospheres and larger humidity variation; similarly, the coastal site TWP3-W also has more significant humidity dilution than its wetter counterparts TWP1 and TWP2.

f. Temperature mixing and b_{E1-m}

We can interpret b_{E1-m} as the temperature mixing aspect of entrainment. From the formulation of b_{E1-m} in Table 2 and appendix B, its derivative with altitude z is approximately proportional to $X(T_e - T_p)$, which means entraining warmer environmental air into the parcel will increase b_{E1-m}; however, warmer temperature also implies less condensation. This results in a different relation between the DC and SC cases, as shown in Fig. 10, compared to components b_c, b_f, and b_{E1-v}, namely, that DC cases tend to have a smaller b_{E1-m} than SC cases. As discussed before, the condensation term b_c significantly decreases because of humidity dilution and temperature mixing. As one aspect of entrainment, the temperature mixing term b_{E1-m} can also influence total buoyancy through altering b_c.

A simple method is adopted to estimate the contribution from temperature mixing on the change of b_c. Besides calculating buoyancy components using the method shown in section 3, we also conducted the same calculation for a second time with a small modification: during the entrainment process of each vertical step Δz, the temperature of the entrained ambient air parcel is changed to a value equal to the parcel temperature right before entrainment. This modification roughly removes the influence on the change of condensation due to temperature mixing. Here, we define $b_{c,\text{ent}} = b_c|_{\text{with entrain}} - b_c|_{\text{no entrain}}$ to represent change of b_c due to entrainment (temperature mixing plus humidity dilution) and $b_{c,\text{ent}-T} = b_{c,\text{ent}} - b'_{c,\text{ent}}$ to represent the change of b_c due to temperature mixing, where the prime denotes the result from our second calculation, which removes the temperature mixing effect mentioned above. Figure 11

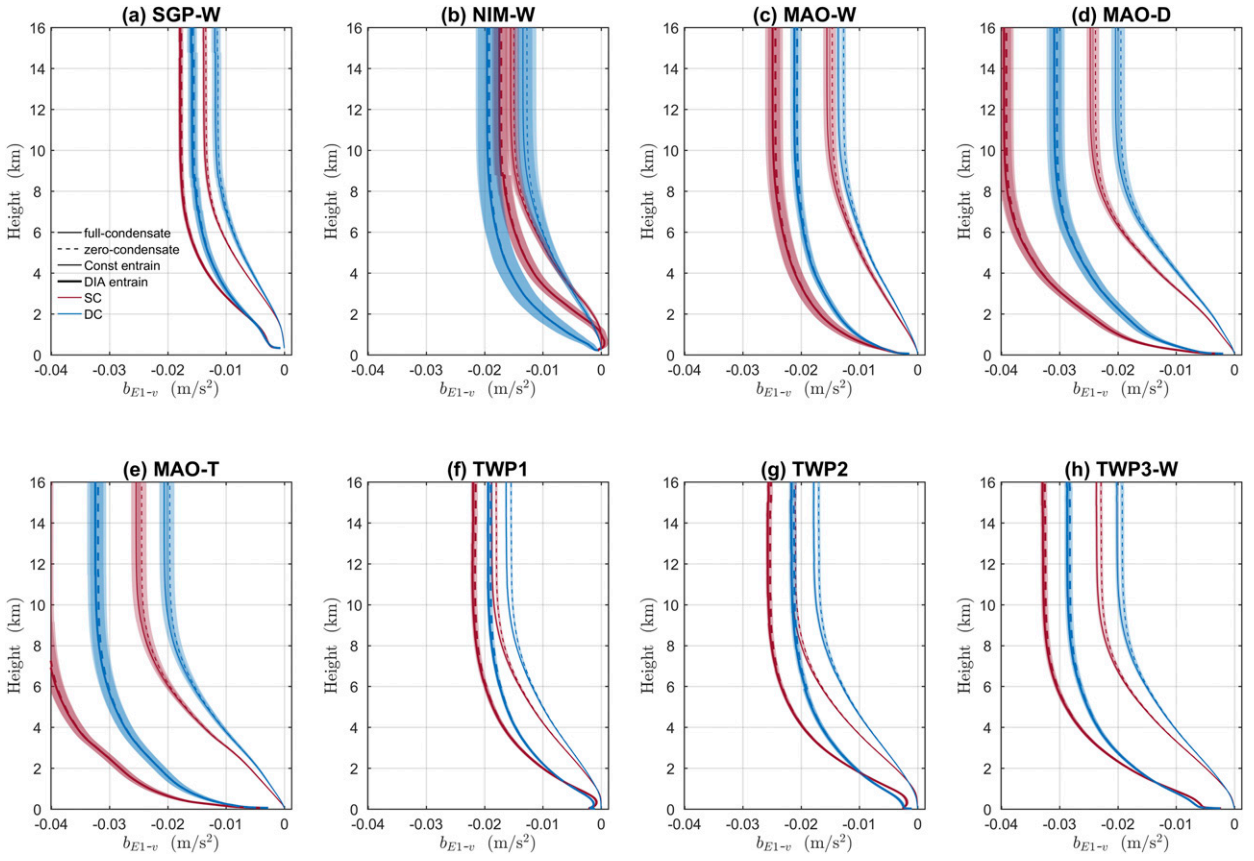

FIG. 9. Composite profiles of the humidity dilution term b_{E1-v} for DC and SC cases and for Const and DIA entrainment schemes at all sites. Shading represents plus and minus one standard error.

shows the composite $b_{c,\mathrm{ent}}$ for two entrainment schemes and for the SC and DC cases. Overall, $b_{c,\mathrm{ent}}$ is negative, meaning that entrainment always tends to reduce condensation; however, the temperature mixing induced by entrainment can either increase or decrease condensation depending on the entrainment scheme and the environmental temperature profiles. Figure 12 shows the ratio of $\Delta b_{c,\mathrm{ent}-T}$ to $\Delta b_{c,\mathrm{ent}}$, where Δ represents the difference between the DC and SC cases. This ratio can be used to indicate the relative contribution from temperature mixing in altering the condensation contrast between DC and SC during the entrainment process. Note that only the value above 4 km is shown since the absolute value of the ratio below ~4 km is much larger than 1 and changes drastically with height at most sites. This is because the absolute buoyancy value is very small in the lower troposphere and the buoyancy's response to the temperature change of entraining air could be amplified substantially. Therefore, the ratio at this level does not reflect the contribution from temperature mixing correctly. The value of $b_{c,\mathrm{ent}}$ is about an order of magnitude larger than $b_{c,\mathrm{ent}-T}$, as expected, since humidity dilution generally has a larger contribution in altering condensation than temperature mixing. However, the ratio shown in Fig. 12 also suggests temperature mixing can still explain about 20%–30% of the difference of $b_{c,\mathrm{ent}}$ between the DC and SC cases. At SGP-W and three TWP sites, $\Delta b_{c,\mathrm{ent}-T}$ is greater with the Const scheme in the middle to upper troposphere than with DIA scheme. However at MAO, $\Delta b_{c,\mathrm{ent}-T}$ tends to be bigger with the DIA scheme than with the Const scheme. This implies that temperature mixing in the lower troposphere has more influence on the shallow-to-deep convection transition at MAO, whereas temperature mixing in the middle to upper troposphere has more influence at SGP-W and TWP.

5. Conclusions and discussion

How the environment influences the shallow-to-deep convection transition and how the relationship varies in different climate regimes are questions fundamental for understanding and adequately modeling the behavior of deep convection globally. However, to our knowledge, a

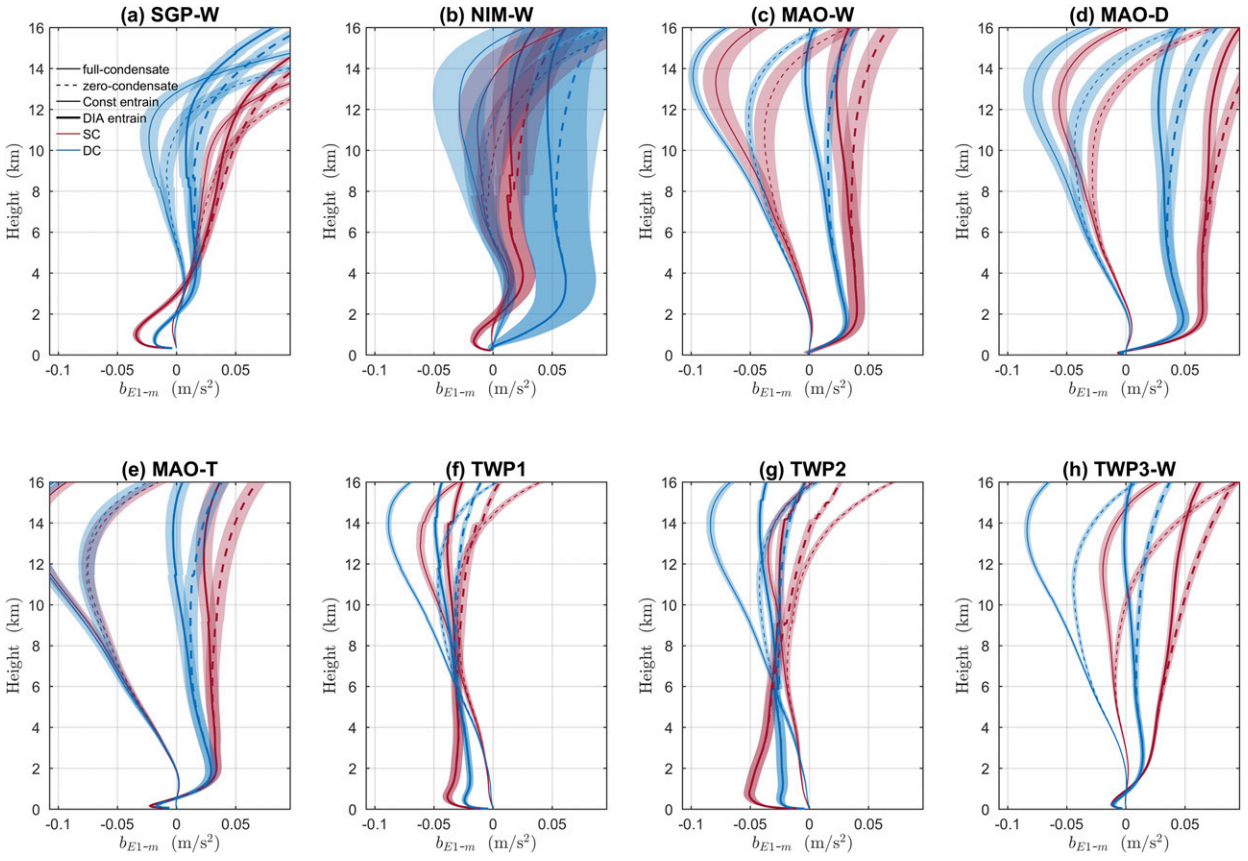

FIG. 10. As in Fig. 9, but for the temperature mixing term b_{E1-m}.

systematic observational assessment as to what controls such variations and what the underlying dominant processes are across different climate regimes has been absent in the literature. This study presents our attempt to address this gap of knowledge for the tropical and subtropical regimes using available observations provided by DOE ARM facilities and field campaigns. To identify the main physical processes behind the observed variations between the environmental preconditions and shallow-to-deep convection transition, we have developed an entraining parcel model to partition buoyancy into several components relative to three main physical processes: moist isentropic ascent, isobaric entrainment, and precipitation. Adding entrainment to buoyancy calculation is one way to include the influence from the atmospheric humidity and temperature profiles above the surface. Using the buoyancy decomposition method, several buoyancy components were analyzed and contrasted between the DC and SC cases in different climate regimes represented by six ARM sites (SGP-W, NIM-W, MAO-W/D/T, TWP1, TWP2, and TWP3-W) to show how environmental conditions can affect the development of convection. Results with three different entrainment schemes (no entrainment, Const entrainment, and DIA entrainment) were compared to show the relative importance of entrainment in different vertical layers. Although the choice of condensate loading scheme (precipitation) can affect buoyancy in the middle to upper troposphere, neither the difference of total buoyancy nor the difference of main buoyancy components between DC and SC cases is changed. The main results about the potential environmental influences for each site are listed in Table 3 based on our analysis for Figs. 6, 9, 10, and 12, where factors with two asterisks appear to be more significant than those with one asterisk . In Table 3, the ABL, lower troposphere (LT), middle troposphere (MT), and upper troposphere (UT) roughly represent vertical layers of 0–1, 1–4, 4–6, and above 6 km, respectively. The main points are summarized below:

1) For the wet season of subtropical continental site SGP-W, surface conditions alone are enough to account for the buoyancy difference between the DC and SC cases due to their large contrast in cloud amount and surface temperature; adding entrainment further enhances the buoyancy contrast but not as significantly as at MAO and TWP.

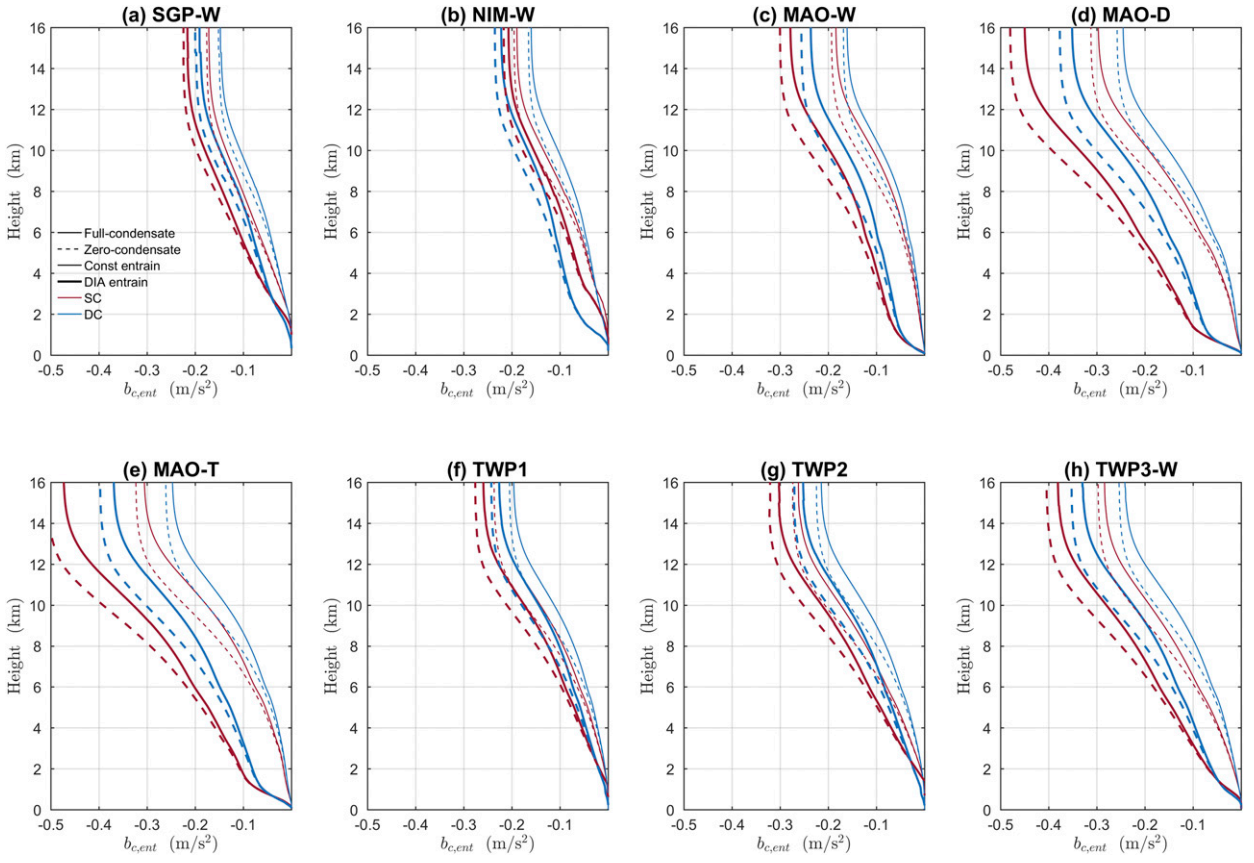

FIG. 11. Composite profiles of $b_{c,\mathrm{ent}}$ (change of the condensation term b_c due to entrainment) for DC and SC cases and for Const and DIA entrainment schemes at all sites.

2) For the monsoonal tropical continental site NIM-W, surface conditions alone are also effective for a positive buoyancy difference between the DC and SC cases; entrainment does not increase the difference. The relatively fewer samples make the conclusion less robust at this site.
3) At the wet tropical continental site MAO, surface conditions in the early morning could be similar for the DC and SC cases. Adding entrainment to the buoyancy calculation is crucial for the DC cases to have larger buoyancy than the SC cases. Decomposition of total buoyancy shows this is mostly because adding entrainment noticeably increases the difference of condensation term b_c between the DC and SC cases. Additionally, the DIA entrainment has a greater effect in increasing the buoyancy difference between the DC and SC cases than does the Const scheme, implying that entrainment in the ABL and the lower free troposphere (~0–4 km) are more important for MAO than at other sites, especially for the dry and transition seasons (MAO-D and MAO-T), when the atmosphere is generally drier and has a larger humidity variation. For the wet season (MAO-W), the temperature mixing effect is shown to have a larger contribution than the other two seasons.
4) For TWP1 and TWP2 surrounded by open ocean, entrainment is necessary for a positive buoyancy difference between the DC and SC cases as at MAO; entrainment in the ABL does not have as significant an impact on the buoyancy difference as at MAO. Humidity dilution in the lower to middle troposphere (~1–6 km) and temperature mixing in the middle to upper troposphere (>4 km) have important influences on increasing the buoyancy difference between the DC and SC cases.
5) For the coastal site TWP3-W, although surface conditions alone are enough for a positive buoyancy difference as at SGP-W, entrainment plays an important role in enhancing the buoyancy difference as seen at the other two TWP sites. Also, the contribution of temperature mixing appears to be larger than at TWP1 and TWP2.

Including entrainment into the calculation of buoyancy provides a way to tie the environmental temperature and

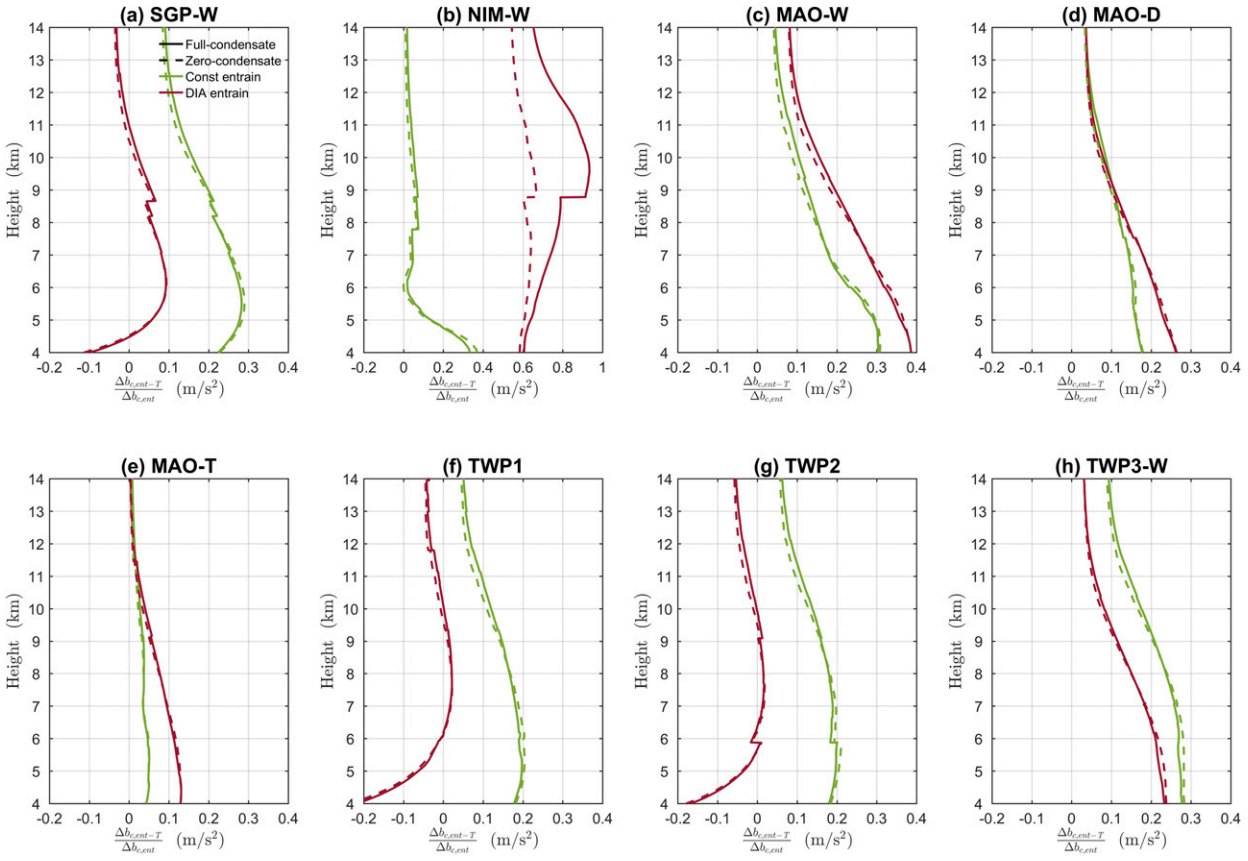

FIG. 12. Composite profiles of $\Delta b_{c,\mathrm{ent}-T}/\Delta b_{c,\mathrm{ent}}$ (contribution of temperature mixing in explaining $b_{c,\mathrm{ent}}$ contrast of between DC and SC cases) for Const and DIA entrainment schemes at all sites.

humidity profiles to convective instability. The fact that involving the entrainment process into buoyancy calculation results in better discrimination between the DC and SC cases agrees well with some main conclusions from previous studies that higher PWV can lead to higher buoyancy (e.g., Holloway and Neelin 2009; Schiro et al. 2016) and more lower-tropospheric humidity can promote shallow-to-deep convection transition (e.g., Zhang and Klein 2010). This study takes one step further to identify the buoyancy component b_c that is most directly related to atmospheric humidity. In addition, the integral of the condensation term $\int_{z_0}^{z_t} b_c\, dz$ was found to be a better instability index for identifying the precondition for the shallow-to-deep convection transition than CAPE or the integral of total buoyancy $\int_{z_0}^{z_t} b\, dz$. Analysis of the correlation between $\int b_f\, dz/\int b_c\, dz$ and PWV shows that the contribution of ice process tends to be larger in a drier environment. This result provides a thermodynamic explanation as to why convection in a drier environment and for a continental region tends to have more ice formation and lightning activities than those in a wetter environment and a maritime region as documented by previous observational studies (e.g., Liu and Zipser 2015; Williams et al. 2002; Zhuang et al. 2017; Zipser et al. 2006).

The buoyancy decomposition method presented in this work is demonstrated to be capable of separating the contributions of different processes to the parcel buoyancy, giving us a new approach to study and understand how thermodynamics influence the development of the convection at different vertical layers, and enabling us to explore the degree to which convective buoyancy is affected by different thermodynamic factors. The results presented in this study are based on observations from six ARM sites, which not only demonstrates the robustness of the results but also allows us to evaluate the variation of the impacts of thermodynamics across different climatic regimes from the subtropics to the tropics, from land to ocean, and from the wet season to the dry season. For example, many observational studies have provided evidence that a moist environment can promote the development of deep convection, especially the low-level moisture (e.g., Holloway and Neelin 2009; Nuijens et al. 2009; Ruppert and Johnson 2015; Zhang and Klein 2010). Our result demonstrates explicitly the influences of the ambient

TABLE 3. Summary of environmental influences on the shallow-to-deep convection transition at different sites. See text for details.

Sites			SGP-W	NIM-W	MAO-W	MAO-D	MAO-T	TWP1	TWP2	TWP3-W
Surface condition			**	**						**
Entrainment	Temp mixing	ABL								
		LT			**	**	**			**
		MT	**			*		**	**	**
		UT	**					**	**	**
	Humidity dilution	ABL			*	**	**			
		LT	*		**	**	**	**	**	**
		MT				*	*	**	**	**
		UT								

temperature and humidity on parcel buoyancy through the entrainment process and shows that this relationship can vary among different regions and seasons. Additionally, this study highlights the importance of improving the representation of entrainment and lateral mixing in parameterization schemes and its impact on shallow-to-deep convection transition.

This approach, however, has some limitations, and more work needs to be done. First, the environmental influences on convection development stated in this study basically refer to the thermodynamic aspects only (temperature and humidity). In reality, many other factors can contribute to the shallow-to-deep convection transition, such as aerosol loading, wind shear, downdraft, large-scale advection and convergence, and detrainment. One focus of our future work will be to evaluate the impacts of these other environmental factors on shallow-to-deep convection transition and so provide an observational basis for improving GCM convection parameterizations by identifying the relative importance of more different physical processes and refining convective trigger functions and closures. Second, as described in section 3, this buoyancy partition method is built using the entraining parcel model. Although this model is more realistic than the traditional isolated-parcel assumption, our treatment of entrainment is still too simple and idealized. In reality, the entrainment process may be more of a stochastic mixing process (Raymond and Blyth 1986, 1992) instead of mixing of a very small parcel with the ambient air. The profile of the fractional entrainment rate is shown to be one of the key factors determining the buoyancy difference between the two convective regimes, but it also varies with different environmental conditions and geographical locations instead of being a prescribed profile as used in this study. For future work, observational study of the entrainment process and refinement of its representation in the parcel model are both needed to gain further understanding of the environmental influence. Additionally, it will be intriguing to utilize this method with both reanalysis and model output from large-eddy simulation (LES) of deep convection to investigate how buoyancy components vary in a diurnal cycle and further verify their relationship to the shallow-to-deep convection transition.

Acknowledgments. We thank the anonymous reviewers for their insightful comments that significantly improved this study and Robert E. Dickinson for editing the final manuscript. Yizhou Zhuang was funded by the China Scholarship Council (CSC; 201506010022) and the startup fund provided to Rong Fu by the University of California, Los Angeles (UCLA). Rong Fu was funded by the GOAmazon project, which is supported jointly by the U.S. Department of Energy (DOE; Grant DE-SC0011117), the São Paulo Research Foundation (FAPESP), and the Amazonas Research Foundation (FAPEAM). Hongqing Wang was funded by the National Natural Science Foundation of China (41275112). All the data used in this study are available through the ARM data archive (https://www.arm.gov/data).

APPENDIX A

List of Symbols

Table A1 shows the definitions, values, and units for the variables and constants in this study.

APPENDIX B

Derivation of the Buoyancy Decomposition Method

In the classic parcel theory, buoyancy is usually defined as

$$b = -g\frac{\rho'}{\rho} \approx -g\left(\frac{p'}{p} - \frac{T_v'}{T_v}\right) \approx g\frac{T_v'}{T_v} = g\frac{T_{pv} - T_{ev}}{T_{ev}}, \quad \text{(B1)}$$

where the virtual temperature of parcel T_{pv} and environment T_{ev} are calculated as

TABLE A1. List of symbols.

Name	Representation	Value/unit
R_d	Gas constant of dry air	287.04 J kg^{-1} K^{-1}
R_v	Gas constant of water vapor	461.5 J kg^{-1} K^{-1}
ε	Ratio of R_d to R_v	0.622
R_m	Gas constant of moist air	J kg^{-1} K^{-1}
c_{pd}	Specific heat of dry air at constant pressure	1005.7 J kg^{-1} K^{-1}
c_{pv}	Specific heat of water vapor at constant pressure	1875 J kg^{-1} K^{-1}
c_l	Specific heat of liquid water	4190 J kg^{-1} K^{-1}
c_i	Specific heat of ice water	2118.636 J kg^{-1} K^{-1}
c_{pml}	Total specific heat of moist parcel (dry air + total water)	J kg^{-1} K^{-1}
c_{pm}	Total specific heat of moist air (dry air + water vapor)	J kg^{-1} K^{-1}
l_{lv}	Latent heat of condensation/vaporization	J kg^{-1}
l_{il}	Latent heat of freezing/fusion	J kg^{-1}
$l_{lv}(T_0)$	Latent heat of condensation/vaporization at 0°C	2 501 000 J kg^{-1}
$l_{il}(T_0)$	Latent heat of freezing/fusion at 0°C	2 836 017 J kg^{-1}
r_t	Total water mixing ratio	—
r_v	Water vapor mixing ratio	—
r_l	Liquid water mixing ratio	—
r_i	Ice water mixing ratio	—
q_t	Total water specific humidity	—
q_v	Water vapor specific humidity	—
q_l	Liquid water specific humidity	—
q_i	Ice water specific humidity	—
T	Temperature	K
θ	Potential temperature	K
X	Fractional entrainment rate	m^{-1}
s	Specific entropy of moist air	J kg^{-1} K^{-1}
s_d	Specific entropy of dry air	J kg^{-1} K^{-1}
s_l	Specific entropy of liquid water	J kg^{-1} K^{-1}
$s_d(0)$	Specific entropy of dry air at 0°C and 1000 hPa	6775 J kg^{-1} K^{-1}
$s_l(0)$	Specific entropy of liquid water at 0°C and 1000 hPa	3517 J kg^{-1} K^{-1}
h	Specific enthalpy	J kg^{-1}
g	Gravitational acceleration	9.81 m s^{-1}
e_{sl}	Water vapor saturation pressure over a plane surface of liquid water	Pa
e_{si}	Water vapor saturation pressure over a plane surface of ice water	Pa
a_{lv}, a_{il}	Affinity	J kg^{-1}
p	Atmospheric pressure	Pa
p_0	Standard pressure	100 000 Pa
p_d	Partial pressure of dry air	$\frac{R_d}{R_d + R_v r_v} p$, Pa

$$T_{pv} = T_p \frac{1 + \varepsilon^{-1} r_{vp}}{1 + r_{tp}} \approx T_p (1 + \varepsilon^{-1} r_{vp})(1 - r_{tp}) \approx T_p [1 + (\varepsilon^{-1} - 1) r_{vp} - (r_{lp} + r_{ip})], \tag{B2}$$

$$T_{ev} = T_e \frac{1 + \varepsilon^{-1} r_{ve}}{1 + r_{ve}} \approx T_e (1 + \varepsilon^{-1} r_{ve})(1 - r_{ve}) \approx T_e [1 + (\varepsilon^{-1} - 1) r_{ve}]. \tag{B3}$$

Substituting (B2) and (B3) into (B1) yields

$$\begin{aligned} b &= g \frac{T_p - T_e + (\varepsilon^{-1} - 1)(T_p r_{vp} - T_e r_{ve}) - T_p r_{lp} - T_p r_{ip}}{T_e [1 + (\varepsilon^{-1} - 1) r_{ve}]} \\ &\approx g \left[\frac{T_p - T_e}{T_e} + (\varepsilon^{-1} - 1) \left(\frac{T_p}{T_e} r_{vp} - r_{ve} \right) - \frac{T_p}{T_e} (r_{lp} + r_{ip}) \right] [1 - (\varepsilon^{-1} - 1) r_{ve}] \\ &\approx g \frac{T_p - T_e}{T_e} + g(\varepsilon^{-1} - 1) r_{vp} - g(r_{lp} + r_{ip}) - g(\varepsilon^{-1} - 1) r_{ve}. \end{aligned}$$

Taking the derivative of buoyancy b against altitude z,

$$\frac{db}{dz} \approx g\frac{d}{dz}\left(\frac{T_p - T_e}{T_e}\right) + g(\varepsilon^{-1}-1)\frac{dr_{vp}}{dz} - g\left(\frac{dr_{lp}}{dz}+\frac{dr_{ip}}{dz}\right) - g(\varepsilon^{-1}-1)\frac{dr_{ve}}{dz}$$
$$= -g\frac{T_p}{T_e}\frac{d\ln T_e}{dz} - g(\varepsilon^{-1}-1)\frac{dr_{ve}}{dz} + \frac{g}{T_e}\frac{dT_p}{dz} + g(\varepsilon^{-1}-1)\frac{dr_{vp}}{dz} - g\left(\frac{dr_{lp}}{dz}+\frac{dr_{ip}}{dz}\right). \quad \text{(B4)}$$

In the above equation, the first two terms on the right-hand side are mostly related to environmental properties: the former is mostly determined by temperature lapse rate, and the latter is determined by mixing ratio lapse rate. The last three terms are related to parcel properties (derivatives of parcel temperature, water vapor, and condensate mixing ratio), and they can be further decomposed according to the three processes mentioned above. By breaking the parcel derivatives into contributions from three processes, and considering total water mixing ratio remains constant during the moist isentropic process $(dr_{tp}/dz)_S = (dr_{vp}/dz)_S + (dr_{lp}/dz)_S + (dr_{ip}/dz)_S = 0$, we have

$$\frac{db}{dz} = \left\{-g\frac{T_p}{T_e}\frac{d\ln T_e}{dz} - g(\varepsilon^{-1}-1)\frac{dr_{ve}}{dz}\right\} + \left\{\frac{g}{T_e}\left(\frac{dT_p}{dz}\right)_S + g\varepsilon^{-1}\left(\frac{dr_{vp}}{dz}\right)_S\right\}$$
$$+\left\{\frac{g}{T_e}\left(\frac{dT_p}{dz}\right)_E + g(\varepsilon^{-1}-1)\left(\frac{dr_{vp}}{dz}\right)_E + g\left[-\left(\frac{dr_{lp}}{dz}\right)_E - \left(\frac{dr_{ip}}{dz}\right)_E\right]\right\} + \left\{g\left[-\left(\frac{dr_{lp}}{dz}\right)_P - \left(\frac{dr_{ip}}{dz}\right)_P\right]\right\}, \quad \text{(B5)}$$

where the subscripts S, E, and P denote moist isentropic ascent, entrainment, and precipitation, respectively. The above four parts enclosed by curly braces represent contributions from the environmental profiles, isentropic ascent, entrainment, and precipitation, respectively.

a. Environmental profiles: $-g\frac{T_p}{T_e}\frac{d\ln T_e}{dz} - g(\varepsilon^{-1}-1)\frac{dr_{ve}}{dz}$

For convenience, we define $db_t/dz = -g(T_p/T_e)(d\ln T_e/dz)$ and $db_r/dz = -g(\varepsilon^{-1}-1)(dr_{ve}/dz)$ to represent contributions from temperature and mixing ratio profiles, respectively.

b. Moist isentropic ascent: $\frac{db_S}{dz} = \frac{g}{T_e}\left(\frac{dT_p}{dz}\right)_S + g\varepsilon^{-1}\left(\frac{dr_{vp}}{dz}\right)_S$

For the moist isentropic ascending process, entropy conservation is equivalent to the following equation derived from Gibbs equation (Hauf and Holler 1987; Tripoli and Cotton 1981):

$$c_{pml}d\ln T - R_m d\ln p + \frac{l_{lv}}{T}dr_v - \frac{l_{il}}{T}dr_i = 0, \quad \text{(B6)}$$

where the specific heat for the moist parcel is $c_{pml} = c_{pml}(r_v, r_l, r_i) = c_{pd} + r_v c_{pv} + r_l c_l + r_i c_i$, and the gas constant for the moist air is $R_m = R_m(r_v) = R_d + r_v R_v$.

From (B6) we can yield

$$\frac{dT}{dz} = \frac{R_m T}{c_{pml}}\frac{d\ln p}{dz} - \frac{l_{lv}}{c_{pml}}\frac{dr_v}{dz} + \frac{l_{il}}{c_{pml}}\frac{dr_i}{dz}$$
$$= \frac{R_d T}{c_{pd}}\frac{d\ln p}{dz} + \left(\frac{R_m}{c_{pml}} - \frac{R_d}{c_{pd}}\right)T\frac{d\ln p}{dz} - \frac{l_{lv}}{c_{pml}}\frac{dr_v}{dz} + \frac{l_{il}}{c_{pml}}\frac{dr_i}{dz}.$$

Thus, the changes of buoyancy terms related to the moist isentropic ascent with height are

$$\frac{g}{T_e}\left(\frac{dT_p}{dz}\right)_S + g\varepsilon^{-1}\left(\frac{dr_{vp}}{dz}\right)_S$$
$$= \frac{g}{T_e}\left[\frac{R_d T_p}{c_{pd}}\frac{d\ln p}{dz} + \left(\frac{R_m}{c_{pml}} - \frac{R_d}{c_{pd}}\right)T_p\frac{d\ln p}{dz} - \frac{l_{lv}}{c_{pml}}\left(\frac{dr_{vp}}{dz}\right)_S + \frac{l_{il}}{c_{pml}}\left(\frac{dr_{ip}}{dz}\right)_S\right] + g\varepsilon^{-1}\left(\frac{dr_{vp}}{dz}\right)_S$$
$$= g\frac{T_p}{T_e}\frac{R_d}{c_{pd}}\frac{d\ln p}{dz} + g\frac{T_p}{T_e}\left(\frac{R_m}{c_{pml}} - \frac{R_d}{c_{pd}}\right)\frac{d\ln p}{dz} + g\left(\varepsilon^{-1} - \frac{l_{lv}}{c_{pml}T_e}\right)\left(\frac{dr_{vp}}{dz}\right)_S + g\frac{l_{il}}{c_{pml}T_e}\left(\frac{dr_{ip}}{dz}\right)_S$$
$$= \frac{db_{S-a}}{dz} + \frac{db_{S-w}}{dz} + \frac{db_{S-c}}{dz} + \frac{db_{S-f}}{dz}.$$

Therefore, we have split the moist isentropic term db_S/dz into four terms: $db_{S-a}/dz = g(T_p/T_e)(R_d/c_{pd})(d\ln p/dz) \approx g(R_d/c_{pd})(d\ln p/dz)$ represents the dry adiabatic ascent, $db_{S-w}/dz = g(T_p/T_e)(R_m/c_{pml} - R_d/c_{pd})(d\ln p/dz) \approx g(R_m/c_{pml} - R_d/c_{pd})(d\ln p/dz)$ represents the heat storage inside all forms of water, $db_{S-c}/dz = g[\varepsilon^{-1} - l_{lv}/(c_{pml}T_e)](dr_{vp}/dz)_s$ represents the latent heat from condensation/vaporization plus the buoyancy correction from liquid water mass change, and $(db_f/dz)_s = (gl_{il}/c_{pml}T_e)(dr_{ip}/dz)_s$ represents the additional latent heat from freezing/fusion when ice process takes place.

c. Entrainment: $\dfrac{db_E}{dz} = \dfrac{g}{T_e}\left(\dfrac{dT_p}{dz}\right)_E + g(\varepsilon^{-1}-1)\left(\dfrac{dr_{vp}}{dz}\right)_E + g\left[-\left(\dfrac{dr_{lp}}{dz}\right)_E - \left(\dfrac{dr_{ip}}{dz}\right)_E\right]$

As entrainment mixing increases entropy of the system, which includes original parcel with entrained ambient air, we do not use (B6) for the decomposition of $(dT_p/dz)_E$. Instead, conservation of enthalpy of the system (original parcel plus entrained ambient air parcel) is assumed since entrainment here is considered as an isobaric process and heat exchange only occurs within the system. For convenience, we also view the entrainment as two subprocesses: the first one is linear temperature mixing without phase change of water; the second one is temperature adjustment due to phase change of water (e.g., reevaporation). We use subscripts $E1$ and $E2$ to denote these two subprocesses, respectively.

For the subprocess $E1$, we have $(dr_{vp}/dz)_{E1} \approx (1/\Delta z)[(r_{vp} + Xr_{ve})/(1+X) - r_{vp}] = [X/(1+X)][(r_{ve} - r_{vp})/\Delta z]$, and $(dr_{lp}/dz)_{E1} + (dr_{ip}/dz)_{E1} \approx (1/\Delta z)[(r_{lp} + r_{ip})/(1+X) - (r_{lp} + r_{ip})] = -[X/(1+X)](r_{lp} + r_{ip})/\Delta z$. The specific enthalpy of the total system before mixing can be written as

$$\begin{aligned} h_0 &= c_{pd}(1-q_{tp})T_p + c_{pv}q_{vp}T_p + c_l q_{lp}T_p \\ &\quad + c_i q_{ip}T_p + c_{pd}X(1-q_{ve})T_e + c_{pv}Xq_{ve}T_e \\ &= c_{pml}T_p + Xc_{pm}T_p, \end{aligned}$$

where $c_{pml} = c_{pd}(1-q_{tp}) + c_{pv}q_{vp} + c_l q_{lp} + c_i q_{ip}$ and $c_{pm} = c_{pd}X(1-q_{ve}) + c_{pv}Xq_{ve}$; and the specific enthalpy after mixing is

$$\begin{aligned} h_{E1} &= (1+X)[c_{pd}(1-q'_{tp})T'_p + c_{pv}q'_{vp}T'_p \\ &\quad + c_l q'_{lp}T'_p + c_i q'_{ip}T'_p] \\ &= (1+X)c'_{pml}T'_p, \end{aligned}$$

where $c'_{pml} = c_{pd}(1-q'_{tp}) + c_{pv}q'_{vp} + c_l q'_{lp} + c_i q'_{ip}$ and the specific humidity of water vapor, liquid, and ice after mixing are $q'_{vp} = (q_{vp} + Xq_{ve})/(1+X)$, $q'_{lp} = q_{lp}/(1+X)$, $q'_{ip} = q_{ip}/(1+X)$. By using enthalpy conservation $h_0 = h_{E1}$, the parcel temperature after mixing T'_p can be calculated as $T'_p = (c_{pml}T_p + Xc_{pm}T_e)/[(1+X)c'_{pml}]$. On the other hand, if we consider a parcel and the ambient air as pure dry air (no water), the enthalpy conservation becomes a simple linear temperature mixing, and the temperature after the dry-air temperature mixing is $T^*_p = (T_p + XT_e)/(1+X)$. Therefore, $(dT_p/dz)_{E1} \approx (T'_p - T_p)/\Delta z = (T'_p - T^*_p)/\Delta z + (T^*_p - T_p)/\Delta z$. And

$$\begin{aligned} \frac{db_{E1}}{dz} &= \frac{g}{T_e}\left(\frac{dT_p}{dz}\right)_{E1} + g(\varepsilon^{-1}-1)\left(\frac{dr_{vp}}{dz}\right)_{E1} + g\left[-\left(\frac{dr_{lp}}{dz}\right)_{E1} - \left(\frac{dr_{ip}}{dz}\right)_{E1}\right] \\ &= \frac{g}{T_e}\frac{T^*_p - T_p}{\Delta z} + \frac{g}{T_e}\frac{T'_p - T^*_p}{\Delta z} + g(\varepsilon^{-1}-1)\frac{X}{1+X}\frac{r_{ve} - r_{vp}}{\Delta z} + g\frac{X}{1+X}\frac{r_{lp} + r_{ip}}{\Delta z} \\ &= \frac{g}{T_e}\frac{\chi}{1+\chi}\frac{T_e - T_p}{\Delta z} + \frac{g}{T_e}\frac{(c_{pml}/c'_{pml} - 1)T_p - \chi(c_{pm}/c'_{pml} - 1)T_e}{(1+\chi)\Delta z} + g(\varepsilon^{-1}-1)\frac{X}{1+X}\frac{r_{ve} - r_{vp}}{\Delta z} + g\frac{X}{1+X}\frac{r_{lp} + r_{ip}}{\Delta z} \\ &= \frac{db_{E1-m}}{dz} + \frac{db_{E1-w}}{dz} + \frac{db_{E1-v}}{dz} + \frac{db_{E1-li}}{dz}. \end{aligned}$$

For the subprocess $E2$, assume temperature and humidity change due to phase change of water are $\Delta T'_p$, $\Delta q'_{vp}$, $\Delta q'_{lp}$, and $\Delta q'_{ip}$. According to conservation of enthalpy, we have $c_{pd}\Delta T'_p + c_{pv}r'_{vp}\Delta T'_p + c_l r'_{lp}\Delta T'_p + c_i r'_{ip}\Delta T'_p = -\Delta r'_{vp}l_{lv} + \Delta r'_{ip}l_{il}$. A Newton–Raphson technique can be used for the calculation of $\Delta T'_p$; $(dr_{vp}/dz)_{E2} \approx \Delta r'_{vp}/\Delta z$, $(dr_{lp}/dz)_{E2} \approx \Delta r'_{lp}/\Delta z$, and $(dr_{lp}/dz)_{E2} \approx \Delta r'_{lp}/\Delta z$ can also be determined according to the weighting technique mentioned before. Considering total water remains constant during this process $(dr_{tp}/dz)_{E2} = (dr_{vp}/dz)_{E2} + (dr_{lp}/dz)_{E2} + (dr_{ip}/dz)_{E2} = 0$, therefore

$$\frac{db_{E2}}{dz}=\frac{g}{T_e}\left(\frac{dT_p}{dz}\right)_{E2}+g(\varepsilon^{-1}-1)\left(\frac{dr_{vp}}{dz}\right)_{E2}+g\left[-\left(\frac{dr_{lp}}{dz}\right)_{E2}-\left(\frac{dr_{ip}}{dz}\right)_{E2}\right]$$

$$\approx\frac{g}{T_e}\frac{\Delta T'_p}{\Delta z}+g\varepsilon^{-1}\left(\frac{dr_{vp}}{dz}\right)_{E2}=g\left(\varepsilon^{-1}-\frac{l_{lv}}{c_{pml}T_e}\right)\left(\frac{dr_{vp}}{dz}\right)_{E2}+\frac{g}{T_e}\frac{l_{il}}{c_{pml}}\left(\frac{dr_{ip}}{dz}\right)_{E2}=\frac{db_{E2-c}}{dz}+\frac{db_{E2-f}}{dz}.$$

Combining the above analyses of two subprocesses of entrainment, we have

$$\frac{db_E}{dz}=\frac{db_{E1-m}}{dz}+\frac{db_{E1-w}}{dz}+\frac{db_{E1-v}}{dz}+\frac{db_{E1-li}}{dz}+\frac{db_{E2-c}}{dz}+\frac{db_{E2-f}}{dz},$$

where $db_{E1-m}/dz=(g/T_e)[(T_p^*-T_p)/\Delta z]$ represents the influence of the simple temperature mixing of dry air, $db_{E1-w}/dz=(g/T_e)(T'_p-T_p^*)/\Delta z$ represents the buoyancy change due to the heat exchange between different forms of water inside the parcel, $db_{E1-v}/dz=g(\varepsilon^{-1}-1)[X/(1+X)](r_{ve}-r_{vp})/\Delta z$ represents the buoyancy change due to the change of water vapor mixing ratio during mixing (no water phase change), $db_{E1-li}/dz=g[X/(1+X)][(r_{lp}+r_{ip})/\Delta z]$ represents the buoyancy change due to change of condensate mixing ratio during mixing (no water phase change), $db_{E2-c}/dz=g(\varepsilon^{-1}-l_{lv}/c_{pml}T_e)(dr_{vp}/dz)_{E2}$ represents the buoyancy change due to latent heat of condensation/vaporization after mixing, plus the buoyancy correction from the corresponding liquid water mixing ratio change, and $db_{E2-f}/dz=g(l_{il}/c_{pml}T_e)(dr_{ip}/dz)_{E2}$ represents the buoyancy change due to latent heat of freezing/fusion during entrainment.

d. Precipitation: $\dfrac{db_P}{dz}=-g\left[\left(\dfrac{dr_{lp}}{dz}\right)_P+\left(\dfrac{dr_{ip}}{dz}\right)_P\right]$

During the precipitation process, it is assumed that a certain amount of condensate falls out without interacting with the parcel. Therefore, the parcel temperature remains unchanged (but the parcel entropy and enthalpy decrease) during this process, and the buoyancy increment is only related to the change of mixing ratio of liquid water and ice condensate.

Two condensate loading schemes were used in this study. The zero-condensate loading scheme assumes all condensates fall out of the parcel during this process ($db_P/dz\geq 0$); the full-condensate loading scheme keeps all condensates inside the parcel ($db_P/dz=0$).

e. Decomposition result

To summarize the above decomposition results,

$$\frac{db}{dz}\approx\frac{db_t}{dz}+\frac{db_r}{dz}+\frac{db_{S-a}}{dz}+\frac{db_{S-w}}{dz}+\frac{db_{S-c}}{dz}+\frac{db_{S-f}}{dz}+\frac{db_{E1-m}}{dz}+\frac{db_{E1-w}}{dz}+\frac{db_{E1-v}}{dz}+\frac{db_{E1-li}}{dz}+\frac{db_{E2-c}}{dz}+\frac{db_{E2-f}}{dz}+\frac{db_P}{dz}. \quad \text{(B7)}$$

Integrating (B7) from surface to altitude z, the buoyancy at altitude z is

$$b=b_t+b_r+b_{S-a}+b_{S-w}+b_{S-c}+b_{S-f}+b_{E1-m}+b_{E1-w}+b_{E1-v}+b_{E1-li}+b_{E2-c}+b_{E2-f}+b_P+b_\varepsilon, \quad \text{(B8)}$$

where b_ε is the error term due to several approximations made above. The representation and mathematical expression for all buoyancy components are summarized in Table 2.

REFERENCES

Ackerman, T. P., and G. M. Stokes, 2003: The Atmospheric Radiation Measurement program. *Phys. Today*, **56**, 38–44, https://doi.org/10.1063/1.1554135.

Altaratz, O., I. Koren, L. A. Remer, and E. Hirsch, 2014: Review: Cloud invigoration by aerosols—Coupling between microphysics and dynamics. *Atmos. Res.*, **140–141**, 38–60, https://doi.org/10.1016/j.atmosres.2014.01.009.

Anber, U., P. Gentine, S. G. Wang, and A. H. Sobel, 2015: Fog and rain in the Amazon. *Proc. Natl. Acad. Sci. USA*, **112**, 11 473–11 477, https://doi.org/10.1073/pnas.1505077112.

Bechtold, P., M. Köhler, T. Jung, F. Doblas-Reyes, M. Leutbecher, M. J. Rodwell, F. Vitart, and G. Balsamo, 2008: Advances in simulating atmospheric variability with the ECMWF model: From synoptic to decadal time-scales. *Quart. J. Roy. Meteor. Soc.*, **134**, 1337–1351, https://doi.org/10.1002/qj.289.

Breidenbach, J. P., D. J. Seo, and R. Fulton, 1998: Stage II and III post processing of NEXRAD precipitation estimates in the modernized weather service. Preprints, *14th Int. Conf. on Interactive Information and Processing System for Meteorology, Oceanography, and Hydrology*, Phoenix, AZ, Amer. Meteor. Soc., 263–266.

Bretherton, C. S., M. E. Peters, and L. E. Back, 2004: Relationships between water vapor path and precipitation over the tropical oceans. *J. Climate*, **17**, 1517–1528, https://doi.org/10.1175/1520-0442(2004)017<1517:RBWVPA>2.0.CO;2.

Chikira, M., and M. Sugiyama, 2010: A cumulus parameterization with state-dependent entrainment rate. Part I: Description and sensitivity to temperature and humidity profiles. *J. Atmos. Sci.*, **67**, 2171–2193, https://doi.org/10.1175/2010JAS3316.1.

Cohen, C., 2000: A quantitative investigation of entrainment and detrainment in numerically simulated cumulonimbus clouds. *J. Atmos. Sci.*, **57**, 1657–1674, https://doi.org/10.1175/1520-0469(2000)057<1657:AQIOEA>2.0.CO;2.

Feng, Z., S. Hagos, A. K. Rowe, C. D. Burleyson, M. N. Martini, and S. P. de Szoeke, 2015: Mechanisms of convective cloud organization by cold pools over tropical warm ocean during the AMIE/DYNAMO field campaign. *J. Adv. Model. Earth Syst.*, **7**, 357–381, https://doi.org/10.1002/2014MS000384.

Frederick, K., and C. Schumacher, 2008: Anvil characteristics as seen by C-POL during the Tropical Warm Pool International Cloud Experiment (TWP-ICE). *Mon. Wea. Rev.*, **136**, 206–222, https://doi.org/10.1175/2007MWR2068.1.

Fulton, R. A., J. P. Breidenbach, D. J. Seo, D. A. Miller, and T. O'Bannon, 1998: The WSR-88D rainfall algorithm. *Wea. Forecasting*, **13**, 377–395, https://doi.org/10.1175/1520-0434(1998)013<0377:TWRA>2.0.CO;2.

Grabowski, W. W., and Coauthors, 2006: Daytime convective development over land: A model intercomparison based on LBA observations. *Quart. J. Roy. Meteor. Soc.*, **132**, 317–344, https://doi.org/10.1256/qj.04.147.

Guichard, F., and Coauthors, 2004: Modelling the diurnal cycle of deep precipitating convection over land with cloud-resolving models and single-column models. *Quart. J. Roy. Meteor. Soc.*, **130**, 3139–3172, https://doi.org/10.1256/qj.03.145.

Hauf, T., and H. Holler, 1987: Entropy and potential temperature. *J. Atmos. Sci.*, **44**, 2887–2901, https://doi.org/10.1175/1520-0469(1987)044<2887:EAPT>2.0.CO;2.

Holloway, C. E., and J. D. Neelin, 2009: Moisture vertical structure, column water vapor, and tropical deep convection. *J. Atmos. Sci.*, **66**, 1665–1683, https://doi.org/10.1175/2008JAS2806.1.

Kollias, P., M. A. Miller, E. P. Luke, K. L. Johnson, E. E. Clothiaux, K. P. Moran, K. B. Widener, and B. A. Albrecht, 2007: The Atmospheric Radiation Measurement Program cloud profiling radars: Second-generation sampling strategies, processing, and cloud data products. *J. Atmos. Oceanic Technol.*, **24**, 1199–1214, https://doi.org/10.1175/JTECH2033.1.

——, ——, K. L. Johnson, M. P. Jensen, and D. T. Troyan, 2009: Cloud, thermodynamic, and precipitation observations in West Africa during 2006. *J. Geophys. Res.*, **114**, D00E08, https://doi.org/10.1029/2008JD010641.

Lin, C. C., 1999: Some bulk properties of cumulus ensembles simulated by a cloud-resolving model. Part II: Entrainment profiles. *J. Atmos. Sci.*, **56**, 3736–3748, https://doi.org/10.1175/1520-0469(1999)056<3736:SBPOCE>2.0.CO;2.

Liu, C. T., and E. J. Zipser, 2015: The global distribution of largest, deepest, and most intense precipitation systems. *Geophys. Res. Lett.*, **42**, 3591–3595, https://doi.org/10.1002/2015GL063776.

Machado, L. A. T., H. Laurent, N. Dessay, and I. Miranda, 2004: Seasonal and diurnal variability of convection over the Amazonia: A comparison of different vegetation types and large scale forcing. *Theor. Appl. Climatol.*, **78**, 61–77, https://doi.org/10.1007/s00704-004-0044-9.

Mather, J. H., and S. A. McFarlane, 2009: Cloud classes and radiative heating profiles at the Manus and Nauru Atmospheric Radiation Measurement (ARM) sites. *J. Geophys. Res.*, **114**, D19204, https://doi.org/10.1029/2009JD011703.

Moran, K. P., B. E. Martner, M. J. Post, R. A. Kropfli, D. C. Welsh, and K. B. Widener, 1998: An unattended cloud-profiling radar for use in climate research. *Bull. Amer. Meteor. Soc.*, **79**, 443–455, https://doi.org/10.1175/1520-0477(1998)079<0443:AUCPRF>2.0.CO;2.

Neggers, R. A. J., A. P. Siebesma, and H. J. J. Jonker, 2002: A multiparcel model for shallow cumulus convection. *J. Atmos. Sci.*, **59**, 1655–1668, https://doi.org/10.1175/1520-0469(2002)059<1655:AMMFSC>2.0.CO;2.

Nuijens, L., B. Stevens, and A. P. Siebesma, 2009: The environment of precipitating shallow cumulus convection. *J. Atmos. Sci.*, **66**, 1962–1979, https://doi.org/10.1175/2008JAS2841.1.

Petersen, W. A., S. W. Nesbitt, R. J. Blakeslee, R. Cifelli, P. Hein, and S. A. Rutledge, 2002: TRMM observations of intraseasonal variability in convective regimes over the Amazon. *J. Climate*, **15**, 1278–1294, https://doi.org/10.1175/1520-0442(2002)015<1278:TOOIVI>2.0.CO;2.

Powell, S. W., and R. A. Houze Jr., 2015: Effect of dry large-scale vertical motions on initial MJO convective onset. *J. Geophys. Res. Atmos.*, **120**, 4783–4805, https://doi.org/10.1002/2014JD022961.

Raymond, D. J., and A. M. Blyth, 1986: A stochastic mixing model for nonprecipitating cumulus clouds. *J. Atmos. Sci.*, **43**, 2708–2718, https://doi.org/10.1175/1520-0469(1986)043<2708:ASMMFN>2.0.CO;2.

——, and —— 1992: Extension of the stochastic mixing model to cumulonimbus clouds. *J. Atmos. Sci.*, **49**, 1968–1983, https://doi.org/10.1175/1520-0469(1992)049<1968:EOTSMM>2.0.CO;2.

Rieck, M., C. Hohenegger, and C. C. van Heerwaarden, 2014: The influence of land surface heterogeneities on cloud size development. *Mon. Wea. Rev.*, **142**, 3830–3846, https://doi.org/10.1175/MWR-D-13-00354.1.

Ruppert, J. H., and R. H. Johnson, 2015: Diurnally modulated cumulus moistening in the preonset stage of the Madden–Julian oscillation during DYNAMO. *J. Atmos. Sci.*, **72**, 1622–1647, https://doi.org/10.1175/JAS-D-14-0218.1.

Schiro, K. A., J. D. Neelin, D. K. Adams, and B. R. Lintner, 2016: Deep convection and column water vapor over tropical land versus tropical ocean: A comparison between the Amazon and the tropical western Pacific. *J. Atmos. Sci.*, **73**, 4043–4063, https://doi.org/10.1175/JAS-D-16-0119.1.

Siebesma, A. P., and Coauthors, 2003: A large eddy simulation intercomparison study of shallow cumulus convection. *J. Atmos. Sci.*, **60**, 1201–1219, https://doi.org/10.1175/1520-0469(2003)60<1201:ALESIS>2.0.CO;2.

——, P. M. M. Soares, and J. Teixeira, 2007: A combined eddy-diffusivity mass-flux approach for the convective boundary layer. *J. Atmos. Sci.*, **64**, 1230–1248, https://doi.org/10.1175/JAS3888.1.

Simpson, J., and V. Wiggert, 1969: Models of precipitating cumulus towers. *Mon. Wea. Rev.*, **97**, 471–489, https://doi.org/10.1175/1520-0493(1969)097<0471:MOPCT>2.3.CO;2.

Soares, P. M. M., P. M. A. Miranda, A. P. Siebesma, and J. Teixeira, 2004: An eddy-diffusivity/mass-flux parametrization for dry and shallow cumulus convection. *Quart. J. Roy. Meteor. Soc.*, **130**, 3365–3383, https://doi.org/10.1256/qj.03.223.

Stokes, G. M., and S. E. Schwartz, 1994: The Atmospheric Radiation Measurement (ARM) program: Programmatic background and design of the cloud and radiation test bed. *Bull. Amer. Meteor. Soc.*, **75**, 1201–1221, https://doi.org/10.1175/1520-0477(1994)075<1201:TARMPP>2.0.CO;2.

Stratton, R. A., and A. J. Stirling, 2012: Improving the diurnal cycle of convection in GCMs. *Quart. J. Roy. Meteor. Soc.*, **138**, 1121–1134, https://doi.org/10.1002/qj.991.

Tao, W. K., J. Simpson, and M. McCumber, 1989: An ice-water saturation adjustment. *Mon. Wea. Rev.*, **117**, 231–235, https://doi.org/10.1175/1520-0493(1989)117<0231:AIWSA>2.0.CO;2.

Tian, Y., and Z. M. Kuang, 2016: Dependence of entrainment in shallow cumulus convection on vertical velocity and distance to cloud edge. *Geophys. Res. Lett.*, **43**, 4056–4065, https://doi.org/10.1002/2016GL069005.

Tokay, A., and D. A. Short, 1996: Evidence from tropical raindrop spectra of the origin of rain from stratiform versus convective clouds. *J. Appl. Meteor.*, **35**, 355–371, https://doi.org/10.1175/1520-0450(1996)035<0355:EFTRSO>2.0.CO;2.

Tripoli, G. J., and W. R. Cotton, 1981: The use of ice-liquid water potential temperature as a thermodynamic variable in deep atmospheric models. *Mon. Wea. Rev.*, **109**, 1094–1102, https://doi.org/10.1175/1520-0493(1981)109<1094:TUOLLW>2.0.CO;2.

Williams, E., and Coauthors, 2002: Contrasting convective regimes over the Amazon: Implications for cloud electrification. *J. Geophys. Res.*, **107**, 8082, https://doi.org/10.1029/2001JD000380.

Wu, C. M., B. Stevens, and A. Arakawa, 2009: What controls the transition from shallow to deep convection? *J. Atmos. Sci.*, **66**, 1793–1806, https://doi.org/10.1175/2008JAS2945.1.

Yang, S., and E. A. Smith, 2006: Mechanisms for diurnal variability of global tropical rainfall observed from TRMM. *J. Climate*, **19**, 5190–5226, https://doi.org/10.1175/JCLI3883.1.

Zhang, Y. Y., and S. A. Klein, 2010: Mechanisms affecting the transition from shallow to deep convection over land: Inferences from observations of the diurnal cycle collected at the ARM Southern Great Plains site. *J. Atmos. Sci.*, **67**, 2943–2959, https://doi.org/10.1175/2010JAS3366.1.

——, and Coauthors, 2008: On the diurnal cycle of deep convection, high-level cloud, and upper troposphere water vapor in the multiscale modeling framework. *J. Geophys. Res.*, **113**, D16105, https://doi.org/10.1029/2008JD009905.

Zhuang, Y. Z., R. Fu, J. A. Marengo, and H. Q. Wang, 2017: Seasonal variation of shallow-to-deep convection transition and its link to the environmental conditions over the central Amazon. *J. Geophys. Res. Atmos.*, **122**, 2649–2666, https://doi.org/10.1002/2016JD025993.

Zipser, E. J., D. J. Cecil, C. T. Liu, S. W. Nesbitt, and D. P. Yorty, 2006: Where are the most intense thunderstorms on Earth? *Bull. Amer. Meteor. Soc.*, **87**, 1057–1072, https://doi.org/10.1175/BAMS-87-8-1057.